Graduate School ETD Form 9
(Revised 12/07)

PURDUE UNIVERSITY
GRADUATE SCHOOL
Thesis/Dissertation Acceptance

This is to certify that the thesis/dissertation prepared

By Todd Randall Dodge

Entitled
EXPERIMENTAL AND COMPUTATIONAL ANALYSIS OF DYNAMIC LOADING FOR BONE FORMATION

For the degree of Master of Science in Biomedical Engineering

Is approved by the final examining committee:

Hiroki Yokota
Chair

Joseph Wallace

Sungsoo Na

To the best of my knowledge and as understood by the student in the *Research Integrity and Copyright Disclaimer (Graduate School Form 20)*, this thesis/dissertation adheres to the provisions of Purdue University's "Policy on Integrity in Research" and the use of copyrighted material.

Approved by Major Professor(s): Hiroki Yokota

Approved by: John Schild 04/17/2013
Head of the Graduate Program Date

EXPERIMENTAL AND COMPUTATIONAL ANALYSIS OF DYNAMIC LOADING FOR BONE FORMATION

A Thesis

Submitted to the Faculty

of

Purdue University

by

Todd Randall Dodge

In Partial Fulfillment of the

Requirements for the Degree

of

Master of Science in Biomedical Engineering

May 2013

Purdue University

Indianapolis, Indiana

ACKNOWLEDGMENTS

I would like to acknowledge my thesis advisor, Dr. Hiroki Yokota, for his invaluable guidance and assistance throughout the course of this thesis project. Dr. Yokota generously shared his passion for experimental research and pursuit of perfection in every detail, and I am very thankful to have been a part of his lab.

I am also very appreciative of my advisory committee members, Dr. Joseph Wallace and Dr. Sungsoo Na, for their time and support during the completion of this thesis.

I extend a special thanks to Dr. Ping Zhang and Dr. Liming Zhao, who each assisted me greatly in the setup and completion of the animals studies that are a part of this thesis. Dr. Zhang is an expert in animal surgery, and without his assistance, the studies with ovariectomized animals would not have been possible. Dr. Zhao contributed greatly to the hindlimb-suspension and *in-vitro* animal studies within this thesis project, and I greatly appreciate the numerous hours he spent training me on many useful lab techniques. I have learned so much from each, and for this I will always be thankful. To them I extend my sincere gratitude.

I would also like to thank Mina Wanis, who spent many hours assisting with the construction of the human-scale knee loading device, and my fellow co-workers Andy Chen and Nancy Tanjung for their technical support and encouragement. I thank Ms. Valerie Lim Diemer for her assistance in formatting this thesis. Finally, I express gratitude to my wife and family for their support and encouragement throughout my academic career, without which this work would not have been possible.

TABLE OF CONTENTS

Page

LIST OF TABLES

LIST OF FIGURES

Figure Page

ABSTRACT

Dodge, Todd Randall. M.S.B.M.E., Purdue University, May 2013. Experimental and Computational Analysis of Dynamic Loading for Bone Formation. Major Professor: Hiroki Yokota.

Bone is a dynamic tissue that is constantly remodeling to repair damage and strengthen regions exposed to loads during everyday activities. However, certain conditions, including long-term unloading of the skeleton, hormonal imbalances, and aging can disrupt the normal bone remodeling cycle and lead to low bone mass and osteoporosis, increasing risk of fracture. While numerous treatments for low bone mass have been devised, dynamic mechanical loading modalities, such as axial loading of long bones and lateral loading of joints, have recently been examined as potential methods of stimulating bone formation. The effectiveness of mechanical loading in strengthening bone is dependent both on the structural and geometric characteristics of the bone and the properties of the applied load. For instance, curvature in the structure of a bone causes bending and increased strain in response to an axial load, which may contribute to increased bone formation. In addition, frequency of the applied load has been determined to impact the degree of new bone formation; however, the mechanism behind this relationship remains unknown.

In this thesis, the application of mechanical loading to treat osteoporotic conditions is examined and two questions are addressed: What role does the structural geometry of bone play in the mechanical damping of forces applied during loading? Does mechanical resonance enhance geometric effects, leading to localized areas of elevated bone formation dependent on loading frequency? Curvature in the structure of bone was hypothesized to enhance its damping ability and lead to increased bone

formation through bending. In addition, loading at frequencies near the resonant frequencies of bone was predicted to cause increased bone formation, specifically in areas that experienced high principal strains due to localized displacements during resonant vibration.

To test the hypothesis, mechanical loading experiments and simulations using finite element (FE) analysis were conducted to characterize the dynamic properties of bone. Results demonstrate that while surrounding joints contribute to the greatest portion of the damping capacity of the lower limb, bone absorbs a significant amount of energy through curvature-driven bending. In addition, results show that enhanced mechanical responses at loading frequencies near the resonant frequencies of bone may lead to increased bone formation in areas that experience the greatest principal strain during vibration. These findings demonstrate the potential therapeutic effects of mechanical loading in preventing costly osteoporotic fractures, and explore characteristics of bone that may lead to optimization of mechanical loading techniques. Further investigation of biomechanical properties of bone may lead to the prescribing of personalized mechanical loading treatments to treat osteoporotic diseases.

1. INTRODUCTION

1.1 Bone: Structure, Function and Adaptation to Loading

Bone is a constantly adapting tissue that is composed of many organic, inorganic, and living components. The primary constituent of bone is a modified version of the inorganic mineral hydroxyapatite, which can comprise more than 50% of the weight of a bone [1]. Bone mineralization occurs when the inorganic hydroxyapatite is deposited along organic collagen fibrils producing the hard matrix of the bone. Type I collagen is the primary organic structural component of bone, and is produced and deposited by osteoblasts, or bone producing cells [2]. However, other types of collagen exist in bone in smaller quantities. Crosslinking between type I collagen fibrils has been shown to be important in the stability and overall strength of bone tissue [3–5]. Other cells found in bone are osteoclasts, or bone absorbing cells, and osteocytes, which function as mechanical sensors within the bone matrix [6].

Bone has numerous mechanical and metabolic functions within the body. Mechanically, bone provides structural support and protection of other organs. Many bones, especially long bones found in the limbs, facilitate movement by providing attachment points for muscles and tendons. The inorganic portion of bone acts as a storage reservoir for minerals important in other body activities, such as calcium and phosphorus. Within the marrow of a bone, located in the intramedullary cavity, production of blood cells occurs in a process called hematopoiesis [7].

The structure of individual bones depends on the location and function of the bone. However, there are two primary types of bone that are common to all bones. Cortical bone forms the outer shell of a bone and makes up 80% of the weight of

the skeleton [8]. Within the cortical shell, the less dense trabecular bone is found. Trabecular bone is oriented in a network of plates and rods that compose a very porous structure. This allows the overall mass of the bone to decrease and provides a space for metabolic processes within the bone, such as blood cell production. On a micro-scale, cortical bone contains numerous pores and channels called lacunae and canaliculae, respectively. These spaces are home to osteocytes and their processes, and are important in the bone remodeling cycle.

The bone remodeling process revolves around the activity of osteocytes, which release sclerostin, a compound that inhibits osteoblast formation by binding low-density lipoprotein receptor-related protein 5 (LRP5) and inhibiting the Wnt signaling pathway in bone. Factors such as mechanical loading of the bone, increases in release of parathryroid hormone (PTH), and the release of some cytokines reduce sclerostin production by osteocytes, initiating bone remodeling. [9]. When bone remodeling is initialized, osteoblasts and osteoclasts are organized into groups called basic multicellular units (BMUs), which first resorb the surface of the bone then deposit new bone in the resorption cavity. When a load is applied to a bone, the matrix of the bone resists the load and is subject to stresses and strains dependent on the type and magnitude of loading. Low strain levels lead to the apoptosis of osteocytes, reducing the activity of osteoblasts and increasing bone absorption by osteoclasts, reducing bone strength over time. A chronic reduction in bone density due to low activity levels may lead to a condition referred to as disuse osteoporosis [10]. Osteoporosis may also be caused by deficiencies in important minerals or hormones, as discussed in the following section.

1.2 Osteoporosis: Symptoms and Causes

Osteoporosis is a condition of reduced bone mass, quality, and strength that leads to increased risk of bone fracture. The World Health Organization defines osteoporosis as the decrease in bone mineral density (BMD) to 2.5 standard deviations below the peak value in a healthy member of a patient's gender [8]. While persons of any age or sex can experience osteoporotic symptoms, osteoporosis is most prevalent in the elderly population, especially in post-menopausal women. Approximately 30% of women and 12% of men will experience osteoporotic symptoms at some point in their lifetime [8]. The greatest threat to an osteoporotic patient, especially the elderly, is bone fracture due to low-impact trauma. In 2010, approximately 530,000 osteoporotic fractures occurred in elderly patients, which cost as much as $16.6 billion to treat [11]. Osteoporotic fractures can be devastating to the health of an otherwise healthy patient, causing debilitating acute and chronic pain and early mortality [12]. Osteoporotic patients may also have a slouched posture due to vertebral compression fractures [13]. Many factors may contribute to the development of low bone mass and osteoporosis. Advanced age, mineral or hormone deficiencies, and long-term disuse are common risk factors.

The single greatest cause of osteoporosis in the general population is advancing age and estrogen deficiency in post-menopausal women. In fact, osteoporosis from this cause is so prevalent that one out of every two women will likely develop low bone mass and increased risk of bone fracture after menopause, which typically occurs around 51 years of age [8]. Estrogens are the primary female sex hormones produced by the ovaries and are important in maintenance of the bone remodeling cycle. Reduction in estrogen concentrations during menopause leads to an elevated number of activated BMUs. However, osteoclast activity is much more prevalent in estrogen-deficient BMUs because of increased recruitment of osteoclasts to bone surfaces and decreased osteoclast apoptosis, leading to longer resorption periods and

larger net bone loss. In addition, removal of estrogens increases the production of inflammatory cytokines, such as interleukin 7 (IL-7) and tumor necrosis factors (TNFs), which inhibit osteoblast activity [14]. Lack of estrogen also decreases intestinal calcium absorption and increases renal calcium loss, requiring the body to free calcium from the bone matrix [8].

Other causes of osteoporosis are less common but may still have debilitating effects. As previously stated, normal mechanical loading of the skeleton that is applied during everyday activities is crucial in the amount of absorption or deposition of bone that occurs during bone remodeling. During periods of disuse or rest, BMUs will tend to absorb more bone and deposit less [15]. The effects of unloading are greatest in bones that normally bear body weight, such as the femur or tibia. For patients that require long term bed rest, or those that suffer a spinal cord injury, this effect is multiplied, and reduction in bone density and strength can become serious [16]. Bone mass has been shown to decrease by up to 6% in the distal tibia in patients on 90-day bed rest [17], and up to 43% in the distal femur in spinal cord injury patients [18]. Certain environments can also lead to reduction in skeletal loading. For astronauts exposed to a micro-gravity environment for a long period of time, normal mechanical loading may be very difficult to achieve. In fact, astronauts in space may lose up to 5.4% of the bone mass in the bones of the leg during a six-month period exposed to micro-gravity [15]. Upon returning to a normal-gravity environment, bones loaded by astronauts and patients coming off bed rest may be at increased risk of catastrophic fracture due to decreased strength. In addition, bone marrow stromal cells may be pushed towards an adipocyte lineage during unloading, inhibiting the recovery of bone when loading resumes [19].

Mechanical properties of bone, such as fracture strength, Young's modulus, or damping capacity, are dependent on both the quantity and quality of bone [2, 10]. BMD is typically used to represent the quantity of bone in a given area, and bone

quality may depend on structural characteristics, such as geometry, in addition to molecular aspects, such as collagen morphology or crosslinking [2, 5]. Osteoporotic conditions have been shown to lead to changes in both the quantity and quality of bone. For example, BMD is decreased in osteoporotic bone, and the morphology of type I collagen has been shown to change [20]. Excessive remodeling and activation of osteoclasts may not allow newly deposited bone by osteoblasts to fully mineralize before being resorbed, reducing the bone's resistance to bending and deformation on a large scale [8]. In addition, the microarchitecture of cortical and especially trabecular bone are modified due to excessive bone remodeling. High levels of bone resorption thin and decrease the numbers of trabeculae in the epiphyses of long bones. Cortical bone also becomes more porous and deteriorates from the endosteal surface, reducing strength [8]. While the micro and nano-scale aspects of osteoporotic bone are important to the overall loss in strength, this study will focus on macro-scale observations of fracture susceptibility, such as Young's modulus and BMD.

1.3 Problem Statement

Osteoporosis is a serious condition leading to the drastic reduction in bone mass in millions of patients in the United States each year. Due to this decrease in bone strength, relatively low-impact falls or loads on affected bones may cause severe fractures of osteoporotic bones [21]. In elderly patients, osteoporotic fractures are especially problematic and may lead to a decline in health and early mortality. An effective treatment to increase bone mass and strength without undesirable side effects would have enormous clinical value and may reduce the chances of catastrophic bone fractures and the accompanying health problems. This thesis proposes dynamic mechanical loading as a treatment for osteoporotic conditions. Understanding the properties of bone under a dynamic load is important in the development of mechanical loading as a treatment method.

1.4 Current and Proposed Treatments

Numerous treatments have been developed to fight the loss in bone density and quality that are characteristic of osteoporotic conditions. Most of these treatments involve administration of a drug or supplement, such as calcium or bisphosphonates, and all treatments involve dietary changes and prevention of falls or impacts to avoid fractures. Minor weight bearing exercise is also used in an attempt to reverse the imbalance in bone remodeling leading to bone loss. However, the use of drugs and supplements may have disadvantages due to adverse side effects. More recent studies have investigated the effects of applied dynamic mechanical loads to the osteoporotic skeleton. While there are currently no FDA approved mechanical loading techniques, these treatment methods show promise in reducing the detrimental effects of osteoporosis.

1.4.1 Drugs and Supplements

Currently, the primary treatment methods for osteoporotic conditions involve dietary changes and administration of supplements to boost the levels of calcium and vitamin D, both important components in bone homeostasis. Since calcium is required by vital body processes, such as in the activation of neurons to produce action potentials, the body will demineralize bones in order to raise plasma calcium concentration if not enough calcium is absorbed from the diet. For this reason, calcium supplements have seen success in studies of osteoporosis treatments. In addition to calcium, supplementation with vitamin D, which helps the body absorb calcium and may have some inhibitory effects on osteoclast precursors, has shown some success in clinical studies [22–25]. However, the beneficial effects of calcium and vitamin D supplementation appear to be limited to patients who already show symptoms of osteoporosis. A 2012 study showed that there is not enough evidence to prove that these supplements prevent fractures in healthy post-menopausal women [26]. In ad-

dition, recent research has shown a link between the use of calcium supplements and increased risk of cardiovascular disease and heart attack [27, 28].

In addition to natural supplements, human hormones or antibodies may be used as antiresorptives to treat osteoporotic bone loss. Denosumab is an FDA-approved antibody that acts as a decoy receptor for receptor activator of nuclear factor kappa-B ligand (RANKL), which is a molecule found on osteoblasts that activates osteoclasts [29]. This antibody mimics the activity of osteoprotegerin (OPG), and inhibits the activation of osteoclasts. Naturally-occuring hormones or modified hormones are also used as anti-resorptives. In post-menopausal women, hormone replacement therapy is commonly used to prevent osteoporotic fractures and reductions in bone mass [30]. However, an increased risk of breast cancer has been noted in long-term hormone replacement therapies [31]. In addition, calcitonin is a naturally occurring hormone that leads to the decrease in osteoclast activity, and has been shown to help prevent osteoporotic fractures in men [32]. Teriparatide consists of the first 34 amino acids of PTH, which when administered intermittently, acts to activate osteoblasts, and has seen some experimental success [33]. While each of these hormones and antibodies may increase mass of osteoporotic bone, side effects, such as kidney stones and osteosarcomas still exist [34].

Other treatments involve the use of synthetic drugs to prevent the loss of bone characteristic of osteoporotic conditions. Three commonly used medications are synthetic vitamin D analogs, bisphosphonates, and strontium ranelate. Vitamin D analogs, which mimic the metabolic activity of vitamin D, have seen success in regulating bone remodeling and may be more effective than vitamin D in increasing bone mass [35, 36]. Another popular class of drugs for osteoporosis treatment is the bisphosphonates, which attach to hydroxyapatite binding sites on the surface of the bone. When osteoclasts degrade the bone matrix containing the drug, the freed bisphosphonate inhibits the ability of the osteoclast to stick to the bone surface and

produce the acids and enzymes required for resorption. Bisphosphonates may also inhibit osteoclast progenitor development and promote osteoclast apoptosis, while preventing osteocyte and osteoblast apoptosis [37]. Collectively, these effects lead to an increase in bone mass [38]. However, treatment with bisphosphonates may have some unintended consequences. For example, since bisphosphonates inhibit the bone remodeling cycle, there is some concern that micro-damage may accumulate in a bone and eventually lead to fracture, even with the increase in bone mass associated with treatment [38]. Perhaps the most significant potential side effect is osteonecrosis of the jaw, which is marked by the exposure and death of bone tissue in the jaw bone or maxillary bone through lesions in the mouth [39]. Strontium ranelate is a strontium salt that mimics the activity of calcium in bone metabolism, allowing the incorporation of strontium atoms into bones. This leads to the increased differentiation of osteoblasts and the inhibition of osteoclasts through increased secretion of OPG. While strontium ranelate has seen lower incidence of adverse side effects than many other therapies, some patients still experience allergic reactions and nausea [40].

1.4.2 Mechanical Loading

Routine mechanical loading is known to maintain the structural integrity of the skeletal system by pushing the bone remodeling cycle towards bone formation rather than resorption [41,42]. Many osteoporosis treatment regimens employ the use of light weight-bearing exercise in an attempt to take advantage of the natural tendency of the skeletal system to adapt to applied loads. However, compliance to these regimens may be poor [43]. For other cases of osteoporosis, such as those caused by disuse, weight bearing exercise may be impossible. For this reason, a method of mechanical loading that requires minimal movement by the patient is desirable.

Many types of applied mechanical loading of the skeleton have been proposed as potential treatments for osteoporotic conditions, including whole body vibration, axial loading or bending of long bones, and lateral joint loading. Each mechanical loading modality is thought to strengthen bone by causing dynamic fluctuations in intramedullary fluid pressure in areas that experience enhanced stresses and strains due to the applied load [41, 44]. This dynamic pressure gradient may cause fluid flow through the lacunocanalicular network of pores in the bone, causing a shear stress to be applied to osteocytes that inhabit those pores and channels. This shear stress may excite the osteocytes, causing activation of osteoblast activity and initiation of the bone remodeling process [44–46]. Mechanical loading may also lead to application of force directly to osteocytes as strain in the bone matrix changes the shape of the lacunae and canaliculae, imposing deformations on the osteocyte and its processes [47, 48].

Whole body vibration (WBV) involves the transfer of energy from a vibrating platform to the entire body of an osteoporotic patient, causing forced oscillations of the bone [43]. A recent clinical study using whole body vibration in addition to an exercise program showed that this treatment method may help to increase bone density in post-menopausal women with low bone mass [49]. Animal studies have also demonstrated a potential osteogenic effect of whole body vibration [19]. However, the limited effectiveness and potential safety concerns associated with this loading modality may cap its use [43].

Other mechanical loading techniques involve the application of force directly to bones or joints. Axial loading creates a bending motion in long bones and may be useful in treating low bone mass in the tibia or ulna. In animal studies of axial loading, increases in cortical and trabecular bone formation were found in tibiae exposed to this loading modality [50, 51]. Lateral loading of joints has also seen success in animal models. For example, loading of the knee joint has been shown to increase bone

formation in the entire length of the femur [52]. Unlike many drugs and supplements, mechanical loading treatments do not have numerous side effects and need only be used for minutes a day.

Many factors may impact the effectiveness of mechanical loading as a treatment for osteoporotic conditions. Properties of the bone, including material characteristics and geometry, may play a role in the anabolic effects of force application. In addition, properties of the load may also impact the degree of osteogenic effects. Depending on the modality, a wide range of frequencies of loading have been implemented in bone loading studies. These frequencies commonly correspond closely to a physiological frequency, such as that of walking or running, in an effort to closely mimic deformations achieved during these activities [53, 54]. Various studies have investigated the role loading frequency plays in bone remodeling and formation, and results indicate that maximum bone formation differs depending on loading frequencies and targeted locations of bones [54–58]. However, the mechanism of this observed frequency dependence remains unknown.

1.5 Objectives

The first objective of this thesis is to investigate the effectiveness of dynamic mechanical loading in reversing the bone loss characteristic of disuse and post-menopausal osteoporosis. To accomplish this, knee loading will be applied to animal models exposed to hindlimb-suspension and ovariectomy (OVX) to simulate skeletal unloading and post-menopausal osteoporosis, respectively. A biomechanical analysis of loading induced bone formation will then be conducted using experimental and numerical methods to investigate the role of the mechanical and geometric properties of the target bone and characteristics of the applied load in osteogenic activity. Curvature-induced bending will be analyzed to determine its impact on the damping capacity

and anabolic bone formation properties of the lower limb. In addition, to help explain an observed frequency dependence of load-driven bone formation, resonance in the structure of the bone will be investigated for its potential stimulatory effects on localized bone formation.

2. DYNAMIC MECHANICAL LOADING OF OSTEOPOROTIC BONES

Normal physical activities, such as walking, running, and jumping increase the strength of bone [41, 59]. These everyday activities and exercises, however, cannot be performed by individuals on bed rest, especially elderly patients. In addition, astronauts in space have limited exposure to mechanical loads. When exposed to these limited-load conditions, individuals may experience disuse osteoporosis in normally-loaded bones, such as the femur and tibia [60, 61]. In addition, bone loss due to post-menopausal estrogen deficiency is a very common affliction increasing the risk of catastrophic bone fracture in millions of women in the United States each year [8]. It is thus useful to develop a mechanical loading method that can easily be used by elderly individuals and astronauts in space. While each type of mechanical loading discussed previously has seen some positive results, joint loading may be the most practical modality to implement in the clinical setting due to lower net force required for the same osteogenic effects as other modalities [45, 62].

In this section, the application of lateral loading of the knee joint to treat osteoporotic bone is studied. Application of load was hypothesized to increase BMD in animals afflicted with osteoporosis caused by both disuse and hormone deficiency. In addition, knee loading was predicted to increase the Young's modulus of compression of an osteoporotic spine, demonstrating a remote increase in the fracture resistance of bone caused by knee loading.

In order to test the hypothesis, animal models of disuse and post-menopausal osteoporosis were utilized. By suspending the tail to a guide wire in the cage, the

rear limbs of mice were unloaded, simulating disuse. Post-menopausal osteoporosis was modeled by surgically removing the ovaries of female mice, mimicking the acute effects of menopause in bone remodeling. These mice present significant increases in bone resorption, together with a slight increase in bone formation [14]. Each model of osteoporosis has been utilized in previous studies [63, 64]. Loading was applied to osteoporotic mice in each group using either a custom-made piezoelectric loading device or an electro-mechanical loading device to apply a dynamic 1 N load to the knee. Changes in bone were quantified by determining BMD of the limb and mechanically determining the Young's modulus of compression for vertebral samples after a loading regimen was complete.

2.1 Experimental Methods

95 C57BL/6 female mice ($\sim$ 12 weeks of age; Harlan Sprague-Dawley, Inc.) were used in these studies (Table 2.1). Experimental procedures were approved by the Indiana University Animal Care and Use Committee and were in compliance with the Guiding Principles in the Care and Use of Animals endorsed by the American Physiological Society.

2.1.1 Hindlimb Suspension

23 wild-type mice were employed in this experiment, in which 12 mice were used for the unloaded (hindlimb-suspended) group and 11 mice used for the control group. The animals were allowed to acclimate for 1 week before the experiment. Mice were anesthetized by inhalation of isoflurane (2.0%), and the tail was inserted into a plastic tube of the tail harness. The animal was placed head-down at approximately a 30 – 40°angle that prohibited the hindlimbs from reaching the ground (Fig. 2.1). The tail harness was attached to a metal swivel (fishing wire) and connected to a metal

Table 2.1

Study Number	Animals	Groups	Description
2-1	23	12 suspended (6 loaded) 11 control (6 loaded)	BMD measured in limbs to evaulate loading effects on suspended animals.
2-2	48	24 OVX (12 loaded) 24 sham (12 loaded)	BMD measured in proximal femur to evaluate loading effects on OVX animals.
2-3	24	12 OVX (6 loaded) 12 sham (6 loaded)	Compressive test conducted on L5 vertebral body to evaluate loading effects on OVX animals.

support that horizontally spanned a housing cage from one corner to the other. The mouse was able to move along the horizontal metal support and access about 80% of the cage. Water (hydrogel placed on floor) and food (placed on floor) were provided ad libitum in a plastic dish throughout the experiment.

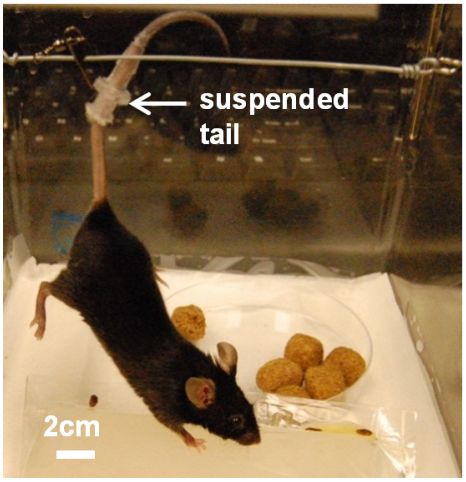

Figure 2.1. Hindlimb suspension model. The tail was suspended in a harness that allowed cage movement, but no weight was allowed on the hind limbs.

2.1.2 Ovariectomy Surgery

In this study, 72 mice were utilized; of which 36 received OVX surgery and 36 received a sham surgery. All animals were weighed prior to ovariectomy and at sacrifice. Anesthesia was conducted with 1.5% isoflurane (IsoFlo, Abbott Laboratories, North Chicago, IL) at a flow rate of 0.5 to 1.0 L/min. The hair at the operative sites (dorsal mid-lumbar area) was shaved, and the skin was cleaned with 70% alcohol and 10% providoneiodine solution. Using a scalpel, a 20 mm midline dorsal skin incision was made. The peritoneal cavity was incised to access the ovaries, which were then excised with scissors. After removing the ovaries, the uterus body was placed back into the peritoneal cavity and the wound was closed by suturing [65,66]. For the sham control

mice, the same procedure was conducted without removing the ovaries. A four-week recovery time was allowed between surgery and administration of mechanical loading.

2.1.3 Knee Loading

Knee loading was utilized to apply dynamic mechanical loads in the medial-lateral direction to the knee joints of hindlimb-suspended, OVX, and associated sham or control animals in each experiment. In each case, the mouse was first placed in an anesthetic induction chamber to cause sedation and then mask-anesthetized using 2.0% isoflurane. Loads were applied to the right knee of 12 hindlimb-suspended and control mice using a custom-made piezoelectric mechanical loader (Fig. 2.2A) [45]. The loading consisted of a 1 N force (peak-to-peak) waveform at 5 Hz for 5 min. The left knee was used as a sham loading control, where the knee was placed under the loading rod for 5 min in the same procedure used for the right knee without applying a voltage signal to the loader. During the procedure tail suspension was temporarily released. However, mice in the tail-suspension group did not receive regular gravity force in their hindlimb since they were anesthetized and laying down. The loading procedure was repeated once each day for 5 days. In the OVX studies, knee loading was applied to both the left and right knees of 36 mice (18 OVX, 18 sham) using a voltage-regulated loading device (ElectroForce 3100; Bose, Inc., Framingham, MA) (Fig. 2.2B). The loading waveform consisted of a 1 N force (peak-to-peak) at 15 Hz for 3 min daily for 10 days (5 days loaded, 2 non-loaded, then 5 loaded). After loading, the animals in each group were allowed to resume normal cage activities.

2.1.4 Measurement of BMD

To measure the BMD of animals in each group, mice were anesthetized in an anesthetic induction chamber and mask-anesthetized using 2.0% isoflurane. A dual-energy

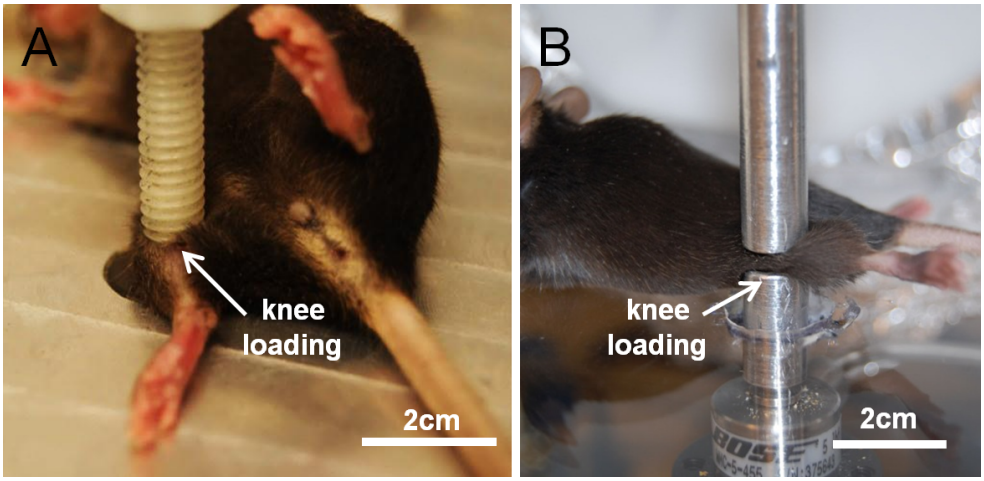

Figure 2.2. Knee loading of hindlimb-suspended and OVX animals. (A) Knee loading was applied to the right knees of hindlimb-suspended mice for 1 week for 5 minutes per day (1 N, 5 Hz) using a custom-made piezoelectric loading device. (B) Knee loading was applied to both the left and right knees of OVX mice 2 weeks for 5 minutes per day (1 N, 15 Hz) using a electro-mechanical loading device (ElectroForce 3100; Bose, Inc., Framingham, MA).

x-ray absorpiometry (Lunar PIXImus 2) machine (GE Medical Systems, Madison, WI), equipped with the Lunar PIXImus 2 software version 2.0, was used to scan the entire body of the mouse. After completion of the scan of the whole body, region of interest boxes were drawn around each limb and the lumbar vertebrae L1-L6 (Fig. 2.5A) of hindlimb-suspended mice, and the femur, tibia, or lumbar vertebrae L1-L6 of OVX mice. BMD (g/cm^2) measurements were obtained from the PIXImus software. In the hindlimb-suspension animals, the left limb (non-loaded) was compared to the right limb (loaded) in each animal. In OVX animals, both limbs of the loaded group were compared to the non-loaded limbs of the OVX control group.

2.1.5 Determination of Young's Modulus

24 mice were utilized to determine changes in Young's modulus of bone due to ovariectomy and mechanical loading; twelve underwent ovariectomy surgery and twelve received a sham surgery. After a 4 week period post-surgery, knee loading of 1 N peak-to-peak at 15 Hz was applied to both the left and right limbs of 6 mice from each group daily (5 days/week) for two weeks. Immediately following euthanasia, the L5 lumbar vertebra was isolated and all soft tissues were removed. The ends of the vertebral body were cleaned to allow as flat of a loading surface as possible. Compressive loading was imposed using an ElectroForce 3100 actuator (Fig. 2.3), and no sample slippage was noted. The loading condition consisted of a ramp function applied at 0.5 N/s to a peak compressive force of 6 N [67]. The maximum load and loading rate were chosen in order to perform a non-destructive test. Young's modulus was determined using the resulting force-displacement relationship and the physical dimensions of each sample [68].

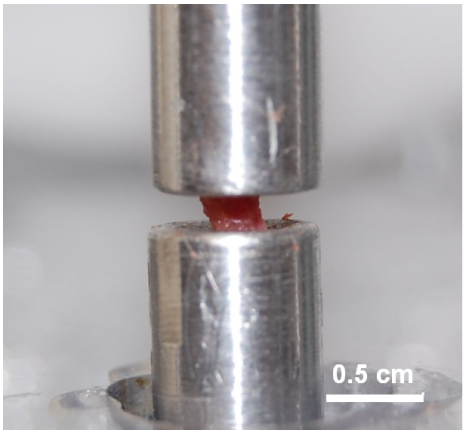

Figure 2.3. Young's modulus of L5 vetebral bodies from OVX, sham, and loaded mice was determined by applying a compressive ramp load using an ElectroForce 3100 loading device. Loading condition was 0.5 N/s in compression to 6 N.

2.1.6 Statistical Methods

The mean and standard deviation of all data was calculated, and 2-way ANOVA was conducted to evaluate statistical significance for cross-comparisons between control vs. suspension, and knee loaded vs. non-knee loaded animals in the hindlimb-suspension study. An unpaired, two-tail Student's t-test was used to determine significance between loaded and non-loaded groups of OVX animals. P-values of less than 0.05 (*) were determined to be significant, with p-values of less than 0.01 (**) and 0.001 (***) denoting higher levels of significance.

2.2 Experimental Results

2.2.1 Post-Experiment Assessment of Hindlimb-Suspended Animals

Upon completion of the hindlimb suspension tests on day 5, animal body weight and BMD were measured. The mean weights of the control and hindlimb-suspended mice were 20.63 g and 18.97 g, respectively, and no statistical difference was observed between the two groups (Fig. 2.4A). The BMD of the whole body and lumbar sections of the animals was measured using PIXImus imaging (Fig. 2.4B). The average BMD of the whole body of control animals was 0.0478 g/cm^2, while the lumbar section exhibited a BMD of 0.0508 g/cm^2. In suspended animals, the average BMD of the whole body was 0.0477 g/cm^2 and the lumbar section was 0.0519 g/cm^2. While a small decrease in BMD was noted in the whole body due to hindlimb suspension, the BMD in each region for both the control and hindlimb-suspended mice was not statistically different.

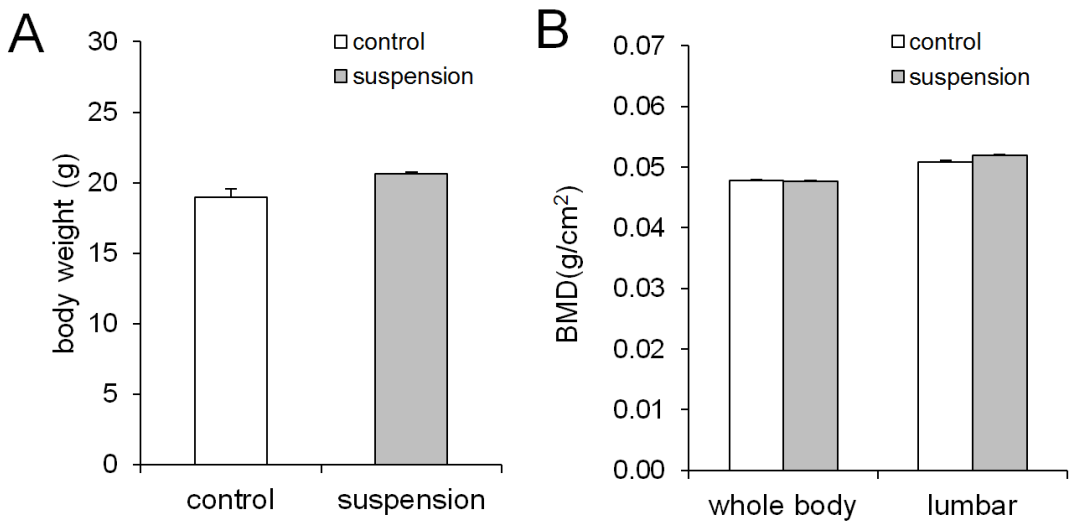

Figure 2.4. Animal assessments after 5 days of hindlimb suspension. (A) Body weight. (B) Whole-body and lumbar BMD.

2.2.2 Effect of Knee Loading on Hindlimb-Suspended Mice

On day 8, PIXImus imaging was used to determine the BMD of the loaded (right) and non-loaded (left) hindlimbs (Fig. 2.5). The BMD of loaded and non-loaded control limbs was found to be 0.0562 g/cm^2 and 0.0524 g/cm^2, respectively, an increase of 7.4% in loaded limbs. In the suspended group, the BMD of loaded and non-loaded limbs was 0.0556 g/cm^2 and 0.0521 g/cm^2, respectively, an increase of 6.6% in loaded limbs. The increases in BMD in loaded limbs were statistically significant ($p < 0.001$) in both the control and suspended animals. A small decrease in BMD was noted in the non-loaded hindlimb of suspended mice compared to the non-loaded control (0.6%), but this difference was not statisically significant. The BMD of loaded limbs in each group was also not statistically different.

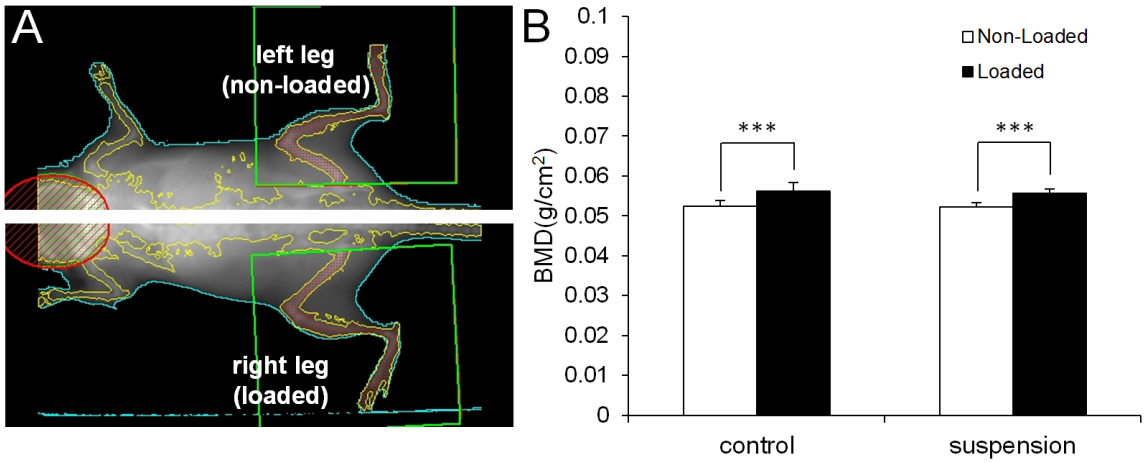

Figure 2.5. BMD measurements of hindlimbs on day 8 using PIXImus imaging (Lunar PIXImus 2; GE Medical Systems, Madison, WI).(A) Regions of interest: left limb (non-loaded) and right limb (loaded). (B) BMD measurements (g/cm^2).

2.2.3 Effect of Knee Loading on OVX Mice

In order to demonstrate bone loss four weeks after OVX surgery, the percent change in whole body BMD and change in BMD of the lumbar spine, femur, and tibia was determined using PIXImus imaging (Fig. 2.6). A decrease in BMD was observed in all areas in OVX animals as compared to animals that underwent a sham surgery. The largest decrease was noted in the lumbar spine, which saw a percent change of approximately -12%. The tibia and femur also showed a decrease in BMD of approximately 3% and 10%, respectively. In total, the average decrease in BMD of the entire body was about 8%. All decreases were statistically significant ($p < 0.001$).

The BMD of the proximal femur of control and OVX mice was measured using PIXImus imaging after two weeks of knee loading (Fig. 2.7). Six weeks after OVX surgery, the average BMD of the proximal femur of OVX mice was 0.046 g/cm^2 in mice that did not receive knee loading. In mice that were exposed to two weeks of

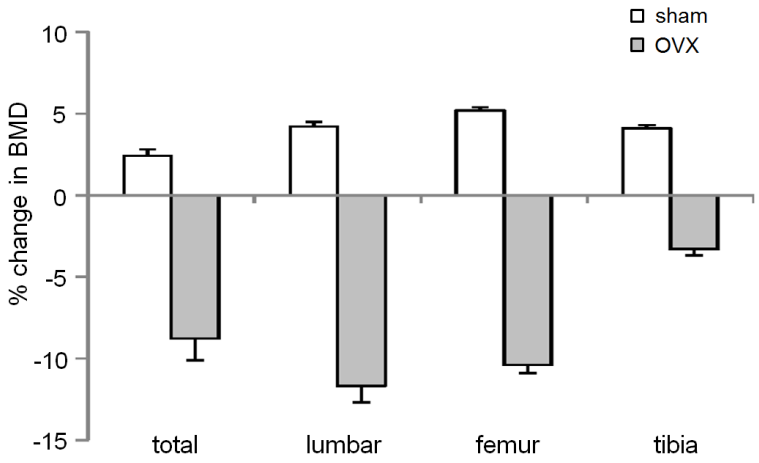

Figure 2.6. Percent change in BMD was determined four weeks after OVX or sham surgery using PIXImus imaging.

daily knee loading, a statistically significant increase in proximal femur BMD to 0.049 g/cm^2 was observed ($p < 0.05$). This change was represented by an increase in BMD of approximately 6.5%.

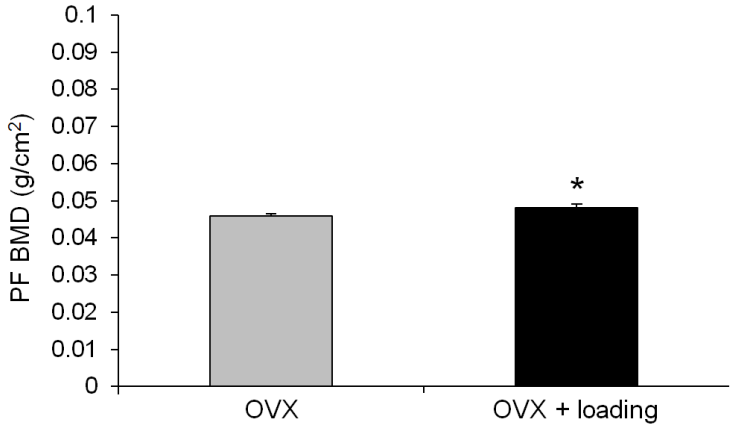

Figure 2.7. BMD of the proximal section of the femur was determined for loaded and non-loaded OVX animals after two weeks of loading.

2.2.4 Young's Modulus of Spine Samples from OVX Animals

Compressive mechanical testing was utilized to determine the compressive Young's modulus of L5 vertebrae isolated from the spine OVX mice and mice that received a sham surgery (Fig. 2.8). A small increase in Young's modulus of 5.9% was noted in normal samples when knee loading was applied, but this difference was not statistically significant. Osteoporotic bone was shown to have greatly reduced mechanical properties, as the Young's modulus of vertebral samples from OVX animals was reduced by approximately 53% compared to normal animals, a statistically significant difference ($p < 0.05$). Interestingly, when knee loading was applied to animals that received OVX surgery, Young's modulus recovered to 324 MPa, or within 0.1% of the normal value, a significant increase of 172 MPa or 112% ($p < 0.05$).

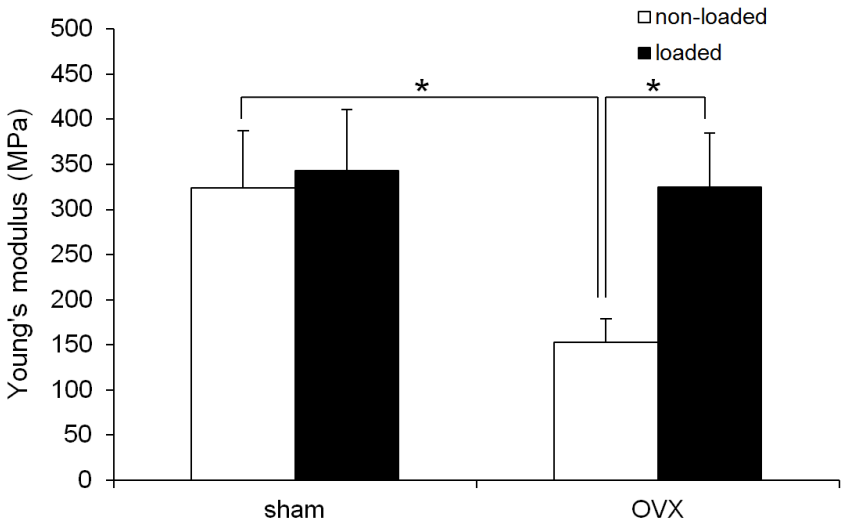

Figure 2.8. Mechanical testing using an ElectroForce 3100 device was used to determine the Young's Modulus of compression of L5 vertebral samples in loaded and non-loaded OVX and sham mice. A 6 N compressive ramp force was applied at 0.5 N/s to the vertebral body and Young's modulus determined using the resulting force-displacement relationship and dimensions of the bone.

2.3 Discussion

The data herein demonstrated that knee loading significantly increased the BMD of hindlimb-suspended ($p < 0.001$) and OVX mice ($p < 0.05$). In addition, the stimulatory effect of knee loading on mice living in a normal, loaded environment noted in previous experiments was confirmed [45, 69], although results show that osteoporotic mice may experience a stronger response.

The mean body weight of hindlimb-suspended mice was not statistically different from the mean body weight of non-suspended mice after day 5 of the study. Although we did not directly measure the amount of food intake, mice appeared to eat and drink properly and were in a healthy condition. In the lumbar spine of the mouse, the mean BMD was slightly higher in hindlimb-suspended mice than in control mice; however, this difference was not statistically significant. The slight increase in BMD in hindlimb-suspended mice may be attributed to additional mechanical stress being applied to the lumbar section of the body, possibly increasing bone growth in that area.

The BMD of mice that underwent 5 days of hindlimb suspension was found to significantly increase by 6.6% in response to knee loading ($p < 0.001$). This increase more than made up for the 0.6% decrease in BMD that was noted in non-loaded limbs after 5 days of hindlimb suspension.

The BMD of mice that underwent OVX surgery to simulate estrogen-deficiency was observed to decrease by up to 12% in the spine, 10% in the femur, and 8% in the entire body compared to those that underwent a sham surgery. In addition, removal of the ovaries was found to decrease Young's modulus of a lumbar vertebral body by 53%. This large discrepancy represents the detrimental effects on mechanical strength that a small decrease in density may cause. Other factors, such as reductions in bone

quality in OVX animals, may contribute to the observed large decrease in Young's modulus [2, 10].

When knee loading was applied to OVX mice, a statistically significant increase in BMD of approximately 5% was noted ($p < 0.05$). While this increase may not completely restore the bone's density to pre-OVX levels, small increases may have a large impact on overall bone strength. Young's modulus of the lumbar vertebrae in OVX animals exposed to knee loading was found to more than double from pre-loading levels. This result suggests that the increase in BMD was not the only factor contributing to the increase in strength in loaded animals, and bone quality aspects may be improved as well.

Since increases in Young's modulus were noted in the spine of knee-loaded animals, mechanical loading may have remote osteogenic properties. Knee loading was able to provide a recovery of Young's modulus in samples from OVX animals to within 0.1% of the normal value, demonstrating a strong positive effect of knee loading in the spine. The decrease in modulus following OVX surgery may have been due to the deterioration of the vertebral structure, since estrogen-deficient bones tend to show increased bone resorption [8, 14]. Increase in modulus may have coincided with increased bone formation due to mechanical loading, recovering the structure of the bone to near pre-OVX levels. Increase in Young's modulus was not statistically significant in normal animals exposed to knee loading, demonstrating that the osteogenic effect is likely stronger in animals that are experiencing increased bone resorption before the initiation of the loading regimen due to estrogen deficiency.

Because the BMD of the non-loaded limb is not statistically different between control and hindlimb-suspended mice, 5 days of unloading may have only been enough to cause a minor case of disuse osteoporosis. A more severe case has been reported in studies utilizing a longer unloading period. For example, after 18 days of hindlimb-

suspension, a decrease in BMD of more than 10% has been noted in the femur of unloaded mice [70]. In addition, after 21 days of unloading, BMD in the femur has been reported to decrease by approximately 15% [71]. While the results are expected to be similar, future studies may employ a longer unloading period to verify the positive effects of knee loading.

This study was performed in various stages over the course of many months. Therefore, loading regimens were altered in later experiments based on available equipment and experimental data. Hindlimb-suspended mice received knee loading from a piezoelectric device, and OVX mice received knee loading from an Electro-Force 3100 device. Regardless of which loading device was utilized to apply the lateral knee loads, the boundary conditions and applied loads were equivalent. Differences involved loading duration and frequency. Loading duration was changed from 5 min per day in hindlimb-suspended animals to 3 min per day in OVX animals based on new data that showed little difference in osteogenic effects between these two durations. Loading frequency was changed from 5 Hz in hindlimb-suspension animals to 15 Hz in OVX animals based on data showing a stronger response in the femur at this frequency [55].

2.4 Conclusions

In summary, mechanical loading significantly increased bone formation and Young's modulus in hindlimb-suspended and OVX mice. The results provide further evidence of the bone-producing capabilities of knee loading by demonstrating that this loading modality can be applied to unloaded and OVX animals as well as animals in normally-loaded environments. Other studies using different forms of mechanical stimulation on hindlimb-suspended mice have had similar results [19]. However, to our knowledge, this study is the first attempt to use knee loading to increase bone formation

in unloaded or OVX mice. Therefore, knee loading may be a suitable mechanical treatment to strengthen bones and help prevent injuries related to osteoporosis.

The results of this study also demonstrate a potential osteogenic effect of bone formation caused by mechanical loading in remote locations away from the load. Previous studies have only investigated bone formation local to the load. In past knee loading studies, for example, increases in bone formation have only been noted in the femur and tibia, and this is the first study to my knowledge to investigate the potentially larger reach of mechanical stimulation. This effect would allow mechanical loading to be applied away from the desired bone formation site, which would be especially important in healing of vertebral fractures, since loading of the spine is difficult to accomplish.

3. BIOMECHANICAL ANALYSIS OF DYNAMIC MECHANICAL LOADING OF BONE

Bone is the strongest, most rigid material found in the body. Because its anisotropic matrix is composed of numerous materials, it tends to exhibit non-linear viscoelastic properties under loading [7, 72]. The brittle hydroxyapatite component contributes to bone's yield strength under constant compressive load, while the elastic collagen component contributes to the tensile strength of bone and allows some displacement after yield until fracture. Under dynamic compressive loading, the non-linear viscoelasticity of bone is also important. When subjected to a dynamic load, bone must be able to absorb and dissipate energy to avoid fracture. The ability of a bone and surrounding tissues to dissipate energy associated with loading, referred to as its damping capacity, is important in maintaining the structural integrity of the bone. Damping capacity may depend on a variety of characteristics of the bone, in addition to the viscoelastic tissues surrounding it [73].

In basic structural mechanics, the structural geometry of an object is important in stress and strain distributions and in the maximum yield strength. Curvature creates a bending motion in an object when a compressive load is applied, and stress concentrations form near the maximum radius of curvature of the object. Therefore, a straight object tends to have higher yield strength in compression than a curved object with the same material properties. In addition, the curved object tends to absorb more energy from loading through the bending motion. Since many long bones have a certain degree of natural curvature, sometimes in many planes and locations, bending may be a contributor to energy dissipation. In addition, due to

the stress concentrations present near the axis of bending, curvature may contribute to enhanced bone formation in response to a dynamic load [51].

In this section, two questions are addressed based on the structural and geometric characteristics of bone. First, what role does the structural geometry of bone play in the mechanical damping of forces applied during loading? Second, does mechanical resonance within the structure of the bone enhance osteogenic geometric effects, leading to localized areas of elevated bone formation dependent on loading frequency? Curvature was hypothesized to enhance a bone's damping ability and lead to increased bone formation through bending. In addition, since bone is a relatively stiff material and has a low damping ratio [74], mechanical loads applied at a frequency near a resonant frequency were hypothesized to enhance bone formation, specifically in areas that experience higher first and third principal strains due to the effects of resonance.

When loading is applied to a stiff material at or near its resonant frequencies, additional energy is absorbed and the material tends to vibrate at greater amplitude than when loading is applied at other frequencies. These vibrations propagate through the material in specific ways, or modes, based on the geometry and characteristics of the material. For a curved object like a bone, resonance may cause enhanced bending motions in multiple planes, depending on the geometry. Finite element (FE) analysis can be used to predict the resonant frequencies and corresponding modes of vibration of an object [75, 76], in addition to expected displacements and strains during vibration.

Many factors may determine the frequencies and modes of vibration of a bone. Material properties and geometry of the bone, along with the assumed boundary conditions, are important aspects [77]. In addition, the complex composition and organization of a typical long bone may also contribute to its frequency response. For

example, the tibia is composed of a shell of dense, stiff cortical bone that is thinnest on the outside of each epiphysis and thickest throughout the diaphysis. Inside the epiphysis a matrix of less dense, weaker trabecular bone is present. An epiphyseal plate is found at the border between the each epiphysis and diaphysis, which consists of hyaline cartilage. Each type of tissue likely contributes to the frequency response of the bone.

To test the hypotheses, animal experiments were conducted and numerical analysis was used to evaluate and verify experimental results. To assess the role of bone in the mechanical damping of applied forces, dynamic loading experiments (tibia loading) were conducted using samples from mouse lower hindlimbs and two damping-related parameters were determined: phase shift angle ($\Delta\Theta$) and energy loss (ΔE) [78, 79]. The phase shift angle was determined as a delay in the phase angle of displacement waveforms to a loading input, while energy loss was calculated as dissipative energy (hysteresis) per loading/unloading cycle. In order to examine the contribution of each of the tissues in the lower hindlimb, loading was applied using five different limb configurations (Samples I – V) in which the tissues such as the skin, foot, knee, and muscle were sequentially removed and the structure was re-tested. Dynamic axial loading was also used to test the effects of resonance in cortical bone formation in the murine tibia. Composite waveforms of low, medium, or high frequency were applied to the lower hindlimb of mice, and volumetric bone mineral density (vBMD) and histomorphometry were used to quantify loading-induced bone formation. Since axial loading has been shown to produce the greatest anabolic effects in cortical bone, especially near the midshaft where bending-induced stresses are largest [50, 51], this experiment focused on cortical bone formation.

To examine a potential effect of bone curvature to load-driven bone formation, we conducted histomorphometric analysis using the tibia in response to axial loading. Because of the tibia's natural curvature, axial loading induces a bending mo-

ment that generates position-dependent stress. Using tibiae from mice loaded with a constant-frequency waveform, we first predicted a curvature-dependent bone deformation throughout the length of the bone as well as the transverse sections at the proximal, middle, and distal regions. We then evaluated any linkage of fluorescently-labeled newly-formed bone surfaces to the predicted bending motion.

To evaluate the experimental data, numerical simulations using a FE model were conducted. A three-dimensional model of the cortical bone component of the murine tibia was constructed using micro-computed tomographical (μCT) imaging and two different analyses were performed. First, the damping ability of the bone with physiological curvature was analyzed by applying dynamic loads of varying frequency to this FE model, and a phase shift angle was determined using the procedure identical for processing experimental data. To evaluate the effect of bone curvature on damping capacity, a secondary model was constructed using dimensions identical to the original model and validated using the physiological radius of curvature. The radius of curvature was then altered between 0 and 150% of the physiological value to examine the effects of curvature on damping capacity. While the tibia has a natural curvature in the medial-lateral and anterior-posterior directions, we focused on the medial-lateral direction of curvature. Second, a modal analysis was executed on model derived from μCT images to investigate the first five resonant frequencies and modes of vibration. Displacements and principal strains (first and third) during vibration were determined, and linkages between observed experimental data and predicted computational results were then evaluated.

3.1 Experimental Methods

Experimental procedures were approved by the Indiana University Animal Care and Use Committee and were in compliance with the Guiding Principles in the

Table 3.1

Study Number	Animals	Groups	Description
3-1	22	18 mice loaded with a 5 N composite axial load, 4 mice used to evaluate damping after euthanasia	Damping analysis of different components of the lower limb.
3-2	3	3 mice loaded with a 1 N, 2 Hz constant frequency axial load	Histomorphometry conducted to evaluate positions of bending-induced bone formation.
3-3	17	6, 7, and 6 mice loaded with low, medium, and high frequency axial tibia load, respectively.	vBMD calculated and histomorphometry conducted to analyze locations of frequency-dependent bone formation.

Care and Use of Animals endorsed by the American Physiological Society. 42 male C57BL/6 mice were used in these studies; 25 ($\sim$ 16 weeks old) were used to evaluate bone curvature and damping of forces in the lower limb and 17 ($\sim$ 13 weeks old) were used to investigate effects of loading frequency on bone formation (Table 3.1).

3.1.1 Tibia Sample Loading for Damping Characterization

To evaluate mechanical damping in the lower limb, tibia loading was conducted to samples from the right lower hindlimb of 18 mice with a voltage-regulated loading device (ElectroForce 3100, Bose, Inc.). The loading regimen was 10 chains of a 5 N (peak-to-peak force) composite waveform consisting of a series of sinusoidal waves at varying frequencies. Each chain was composed of one cycle of the waves at 0.5 Hz and 1 through 20 Hz (1 Hz increments). These waves were connected at the highest peak, where the slope of each sinusoidal wave was equal to zero.

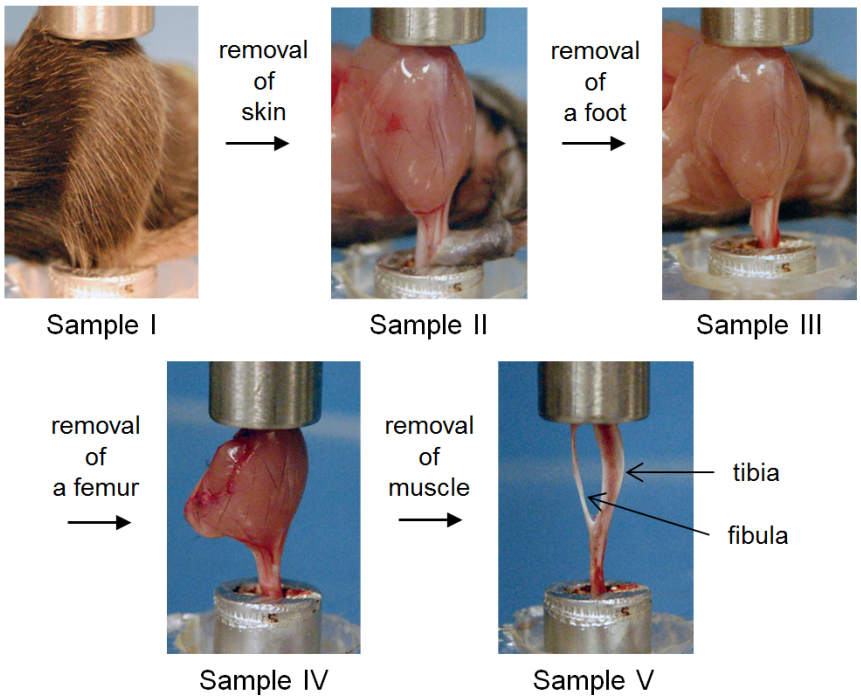

Figure 3.1. Experimental sample configurations I- V for tibia loading: I – intact lower hindlimb; II - limb without skin; III - limb without skin and foot; IV - limb without skin, foot, and femur; and V – limb without skin, foot, femur, and muscle.

Loading was applied to five different sample configurations I - V (Fig. 3.1). Those configurations were the intact lower hindlimb (Sample I), the limb without skin (Sample II), the limb without skin and foot (Sample III), the limb without skin, foot, and femur (Sample IV), and the tibia and fibula alone without an intact joint on either end, and having the surrounding soft tissues (e.g. musculature) removed (Sample V). Sample I was prepared from four additional anesthetized and euthanized animals, and the temporal change of phase shift angles after euthanasia was evaluated. Samples II - V were prepared only from the euthanized animals within 20 min after euthanasia.

3.1.2 Determination of Phase Shift Angle and Energy Loss

Phase shift angles between applied sinusoidal forces and displacements of the lower hindlimb were determined. Force (f) and displacement (L) were modeled as a sinusoidal wave:

$$f = A_f sin(\omega t + \Theta_f) + B_f \tag{3.1}$$

$$L = A_L sin(\omega t + \Theta_L) + B_L \tag{3.2}$$

The phase shift angle was determined as $\Delta\Theta = \Theta_f - \Theta_L$ using a least square-mean fit method with MATLAB software (version 7.10, MathWorks, Inc., Natick, MA). In response to a sinusoidal force waveform at 0.5 Hz, 2 Hz, and 20 Hz, energy loss, ΔE, was determined as a hysteresis loop integral.

3.1.3 Phase Shift Angle of the Loading System

Prior to testing sample configurations I – V, the phase shift angle induced by the loading device itself was evaluated. Between the aluminum base and axial mover, a

straight steel rod (20 mm long, and 3 mm in diameter) was placed. The phase shift angle of this configuration was treated as the contribution of the loading system.

3.1.4 *In-vivo* Axial Tibia Loading

Three mice were used for tibia loading for histological analysis to determined bending-induced effects on bone formation. The mouse was placed in an anesthetic induction-chamber to induce sedation and mask-anesthetized using 2.0% isoflurane. Using the ElectroForce 3100 loading device, axial loads of 5 N were applied at 2 Hz for 3 min per day for 3 consecutive days to the left tibia. The non-loaded right tibia was treated as a contralateral control. Mice were given an intraperitoneal injection of alizarin at 50 μg/g on day 5, and calcein at 30 μg/g on day 11. Animals were sacrificed 13 days after the last loading and the tibiae harvested for histological analysis. The isolated bones were cleaned of soft tissues and fixed with 10% neutral buffered formalin. They were embedded in methyl methacrylate, and the transverse sections were removed from the proximal (25%), middle (50%), and distal (75%) regions along the length of the tibia.

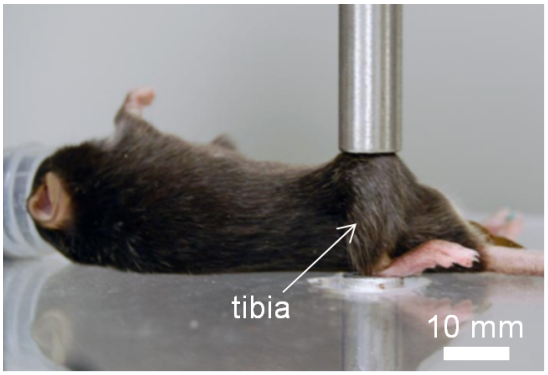

Figure 3.2. Tibia axial loading configuration for application of waveforms of varying frequency ranges.

To study the effects of varying loading frequency ranges on bone formation in the murine tibia, axial tibia loading was applied to the lower right hindlimb of 16 mice with the ElectroForce 3100 loading device. The mouse was placed in an anesthetic induction chamber to cause sedation and then mask-anesthetized using 2.0% isoflurane (Fig. 3.2). Axial loading was applied to the right tibia daily for two weeks (5 days loaded, then 2 non-loaded, then 5 loaded). The left tibia of each mouse was used as a non-loaded contralateral control. The loading condition consisted of a 7 N (peak-to-peak force) composite waveform comprised of a series of sinusoidal waves from a low, medium, or high frequency group (Fig. 3.3). The low frequency group, consisting of 6 animals, was exposed to a loading waveform that began at 1 Hz and increased consecutively by a 1 Hz increment to 17 Hz. The medium group covered the range of 18 Hz to 34 Hz (1 Hz increment) and utilized 5 animals. Six animals underwent high frequency loading, which consisted of a loading waveform beginning at 35 Hz and increasing consecutively by a 1 Hz increment to 51 Hz. Each composite waveform consisted of one cycle of each frequency (from minimum to maximum) in the group combined consecutively at the peak of each wave. To ensure continuity, the composite waveform immediately following was reversed. Each loading group received 200 repetitions of each frequency in the low, medium, or high range daily.

3.1.5 Peripheral Quantitative Computed Tomography (pQCT)

To determine the vBMD of tibiae loaded with waveforms of varying frequency, pQCT was employed (XCT Research SA Plus, software 5.40; Norland- Stratec Medizintechnik GmbH, Birkenfel, Germany). Tibiae from loaded and non-loaded limbs were harvested and fixed in 10% neutral buffered formalin. Sections at 8%, 33%, 50%, and 66% of the length of the bone from the proximal end were scanned at five consecutive cross-sections with a sectional distance of 0.4 mm, where each section was 260 µm in thickness with a voxel size of 70 µm (source current: 300 μA; source voltage:

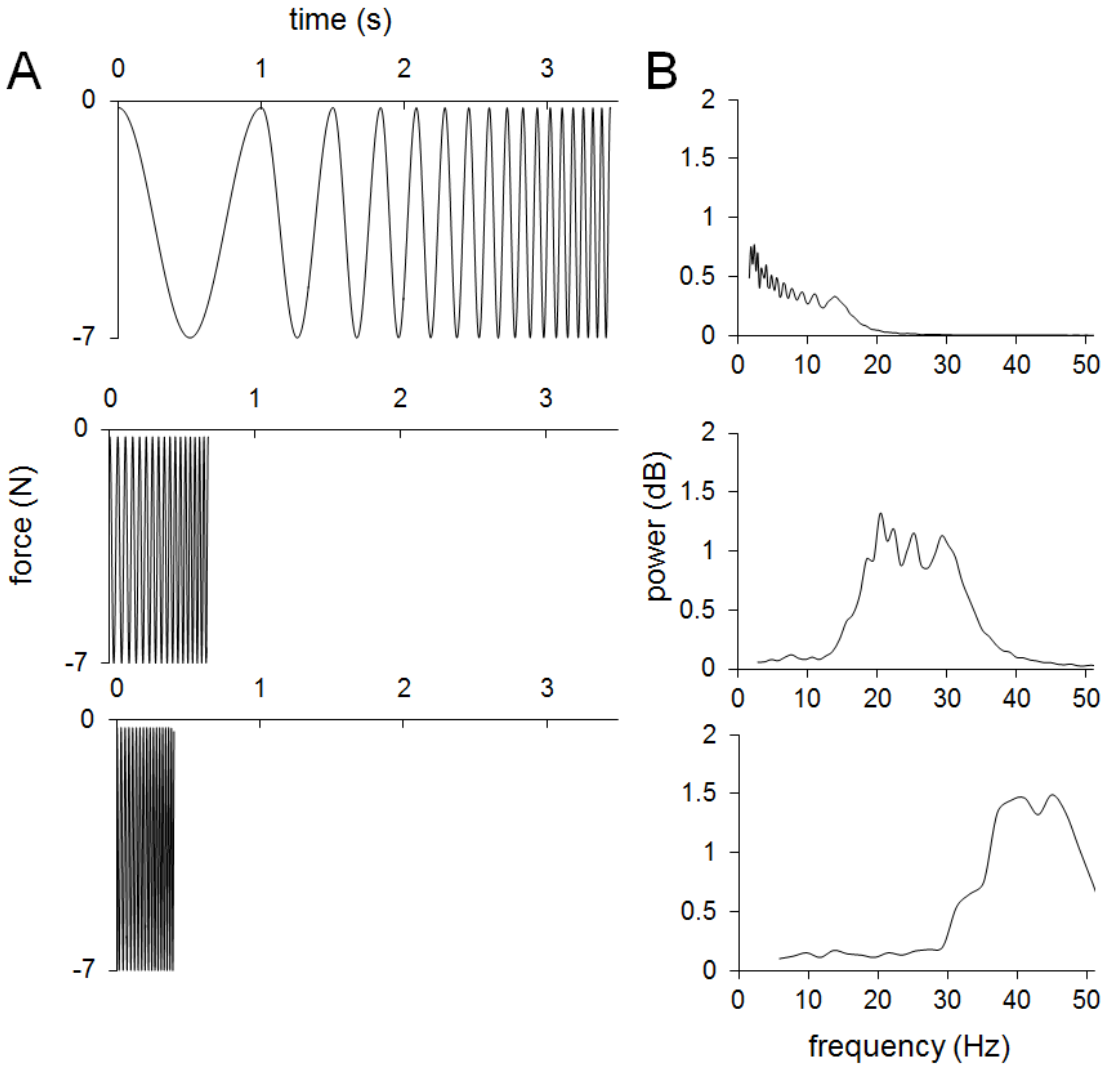

Figure 3.3. (A) Graphical representation of the low frequency, medium frequency, and high frequency loading waveforms applied axially to the tibiae of mice. (B) Power spectrum of the loading waveforms.

50 kV; 105 μ Cu filter). Scans were analyzed for total density at a threshold of 710 mg/cm^3 using manufacturer provided software. Data was presented as the change in vBMD (ΔvBMD), which is defined as the difference in vBMD between the loaded (right) and the non-loaded control (left) tibiae, such that $\Delta vBMD = loaded - non\text{-}loaded$.

3.1.6 Bone Histomorphometry

To study locations of maximum bone formation due to variable-frequency axial loading, 0.6% calcein (30 mg/kg body mass; Sigma Chemical Co., St. Louis, MO) and 1.0% alizarin (50 mg/kg body mass; Sigma Chemical Co., St. Louis, MO) were injected 8 and 3 days prior to euthanasia, respectively, to each mouse in all loading and control groups. After euthanasia, specimens were dehydrated in a series of graded alcohols and embedded in 99% methyl methacrylate with 3% dibutyl phthalate (Aldrich Chemical Co., Milwaukee, WI). Transverse sections (20 – 30 µm in thickness) at 8% and 66% locations along the length of the tibia were removed using a diamond-embedded wire saw (Histo-saw, Delaware Diamond Knives, Wilmington, DE) [80–82]. After polishing the surface, sections were mounted on standard microscope slides. Total perimeter, endocortical perimeter, single-labeled perimeter, double-labeled perimeter, and double-labeled area were measured, and the ratio of labeled surface to total bone surface (LS/BS) [83] was determined using OsteoMeasureXP analysis software (version 3.2, OsteoMeasure, Inc., Decatur, IL) on an Olympus fluorescent microscope (model BX53F, Olympus America Inc., Center Valley, PA). Data was presented as the change in LS/BS (ΔLS/BS), which is defined as the difference in LS/BS between the loaded (right) and the non-loaded control (left) tibiae, such that $\Delta LS/BS = loaded - nonloaded$.

3.1.7 FE Model from μCT Images of the Murine Tibia

MicroCT images of an isolated murine tibia were produced using a Scanco VivaCT 40 imaging machine (Scanco Medical AG, Wayne, PA). The images were reconstructed into a three-dimensional mesh using MIMICS 13.1 (Materialise, Inc., Leuven, Belgium), in which the model was decomposed to approximately 10,000 tetrahedral units (Fig. 3.4). The three-dimensional mesh was imported into COMSOL Multiphysics software (version 4.2; COMSOL Inc., Burlington, MA) for analysis. Material

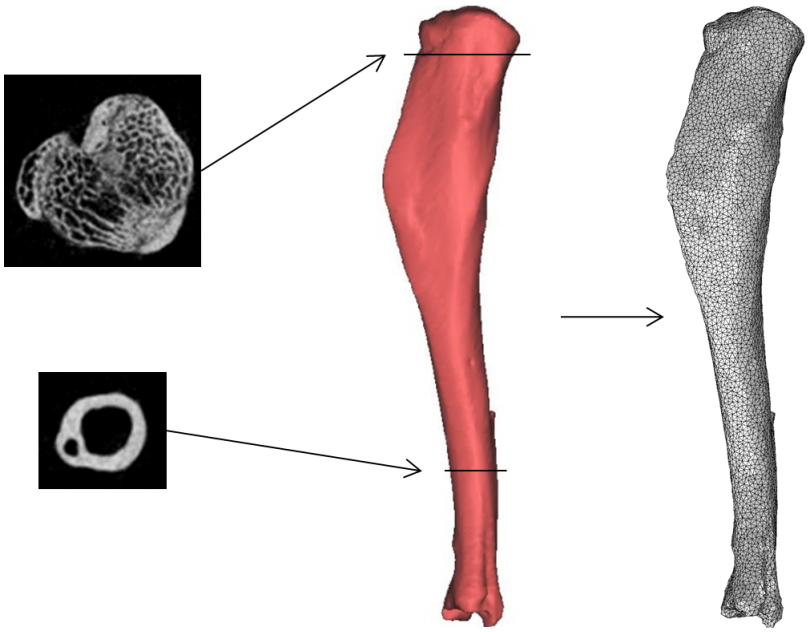

Figure 3.4. A FE model of the murine tibia was created by first producing μCT images (Scanco VivaCT 40; Scanco Medical AG, Wayne, PA). A 3-D reconstruction of the images was created and remeshed using MIMICS 13.1 software (Materialise, Inc., Leuven, Belgium). This model was imported into COMSOL Multiphysics software (version 4.2, COMSOL Inc., Burlington, MA).

properties of cortical bone, such as Poisson's' ratio, Young's modulus, and density, were obtained from literature and pQCT data [74, 84, 85]. Values used for these constants were 0.35, 8.9 GPa, and 1,167 kg/m^3 for Poisson's ratio (ν), Young's modulus (E), and density (ρ), respectively.

3.1.8 FE Analysis of Geometric Damping Effects

Dynamic loads of 5 N in a sinusoidal waveform at 0.5, 2, and 20 Hz were applied normal to the proximal end of the μCT FE model for 10 sec, while the distal end was

pinned to simulate experimental conditions. The phase shift angle was determined using the same procedure as for analyzing experimental data.

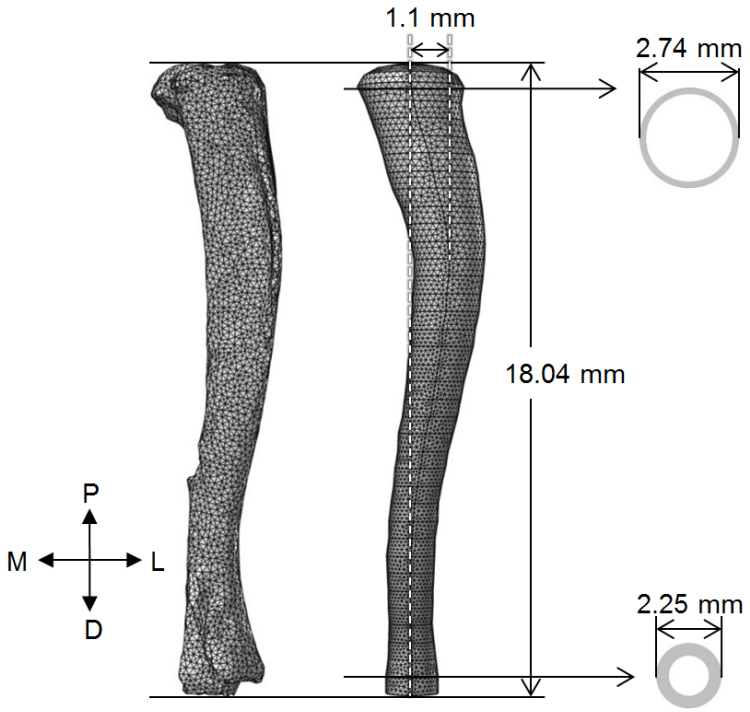

Figure 3.5. A model derived from μCT scans of a tibia (left) was used to create a FE model with the same dimensions and radius of curvature as the original tibia. Cross sections from the proximal and distal parts of the model demonstrate the interior structure of the cortical bone. The letter labels are: M - medial; L - lateral; P - proximal; and D - distal.

A secondary three-dimensional FE model of the tibia, built using the dimensions and radius of curvature derived from the μCT images obtained for the first model, was constructed using COMSOL Multiphysics software (Fig. 3.5, right). Radius of curvature (d) was defined as the maximum distance between the central axis of the bone and an imaginary axis spanning the center of the two ends of the bone. The same material properties used in the μCT FE model were also used in this model. Using a physiological radius of curvature, results were compared between the two FE models to validate the secondary model. To evaluate any effect of bone curvature

on mechanical damping, the radius of curvature of the secondary tibia model was altered between 0 and 150% the original value to determine the effect of curvature on mechanical damping in the tibia, creating a total of 5 new models (Fig. 3.6). Dynamic loads of 5 N in a sinusoidal waveform at 0.5, 2, and 20 Hz were applied normal to each tibia model for 10 sec, and a phase shift angle was determined using the procedure identical for analyzing experimental data.

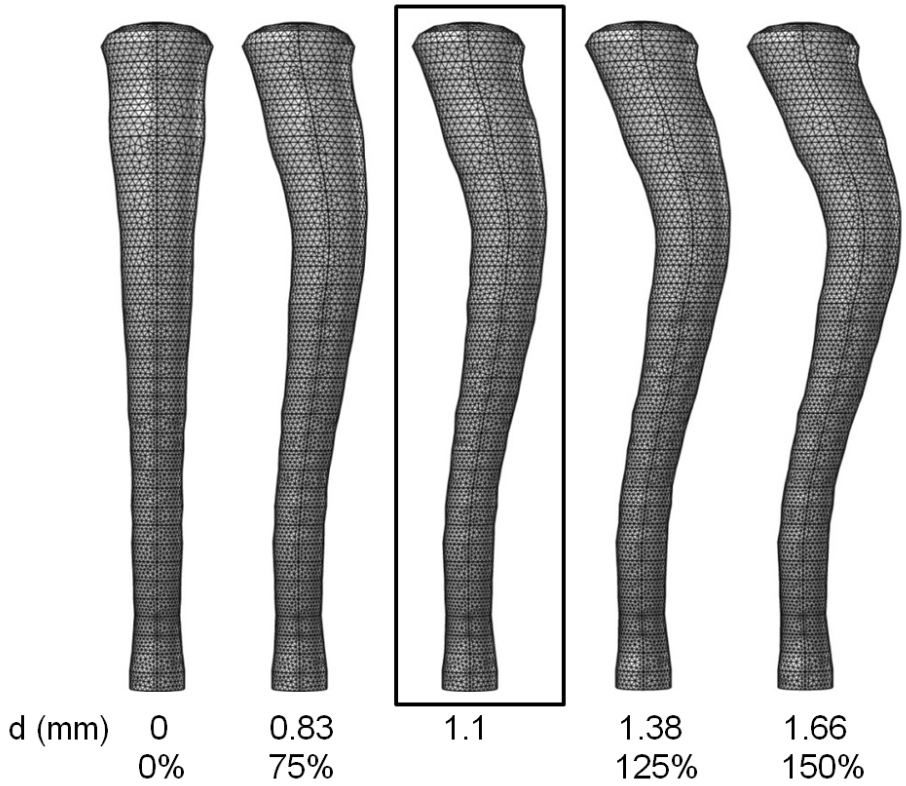

Figure 3.6. Additional FE models of the tibia were created by changing the radius of curvature of the secondary FE model of the tibia (boxed) to values 25% and 100% lower, along with 25% and 50% higher.

3.1.9 Numerical Modal Analysis of the Tibia FE Model

To determine the first five resonant frequencies and modes of vibration of the murine tibia, modal analysis of the FE model derived from μCT images was conducted using COMSOL Multiphysics software. In order to closely simulate physiological conditions, two boundary conditions were set by "pinning" the bone at the ends by restricting the movement of elements on the surface of the knee joint and ankle joint. A built-in eigenfrequency solver was used to determine the first five frequencies and modes of vibration of the tibia model. Post-processing of the model data allowed determination of distributions of first and third principal strains for each of the vibrational modes.

In order to quantify the locations of maximum principal strain predicted by the FE model, an average strain was calculated at the 8% and 66% level for each of the first five vibrational modes of the tibia. In each location, the sum of the principal strain value at each node of the FE mesh was divided by the total number of nodes in the section to obtain an average strain within that section. The relative strain between locations was calculated by dividing the average principal strain in the 8% location by the average principal strain in the 66% location. This ratio was calculated for each the first and third principal strain distributions.

3.1.10 Statistical Considerations

The mean and standard deviation of all data were calculated, and the Student's t-test was used to determine statistical significance. Since all comparisons were made between samples originating from different animals, an unpaired two-tailed t-test was utilized. P-values of less than 0.05 (*) were determined to be significant, with p-values of less than 0.01 (**) denoting a higher level of significance.

3.2 Experimental Results

3.2.1 Loading System Contribution to Damping and Post-Mortem Time Dependency

The loading system was evaluated with anesthetized and euthanized animal models. The phase shift angle, induced by the loading device without any animal sample, was 1.1°at 0.5 Hz, 1.3°at 2 Hz, and 2°at 20 Hz. These angles were induced by the loader itself and removed from the contributions of bone and surrounding tissues. With animal samples, the phase shift angles for the sample configuration I gradually decreased after euthanasia (Fig. 3.7). In response to the loading at 0.5 Hz, for instance, the ratio of measured phase shift angles in euthanized animals to anesthetized animals decreased from 0.99 immediately after euthanasia to 0.96, 0.89, and 0.81 after 20 min, 40 min, and 60 min, respectively, due to the natural post-mortem increase of stiffness. This time-dependent alteration of mechanical properties was found to lower the damping capacity of the intact hindlimb, potentially decreasing the observed phase shift angle of sample configurations I through IV in the following experiments. For this reason, in the experiments that required euthanized animals, we employed animals within 20 min after euthanasia to reduce the effects of post-mortem time-dependent alterations of mechanical response.

3.2.2 Determination of Phase Shift Angles

In response to axial loading of lower hindlimb samples, the representative force and displacement responses are depicted (Fig. 3.8). Loads were 5 N (peak-to-peak) in a series of individual sinusoidal components, including the frequencies 0.5 Hz and 1 through 20 Hz, at 1 Hz intervals. Loading at 0.5 Hz for sample configurations I and V generated displacements of 0.42 and 0.08 mm, respectively (Fig. 3.8A, 3.8B). At 2 Hz, sample configurations I and V produced displacements of 0.38 and 0.06 mm,

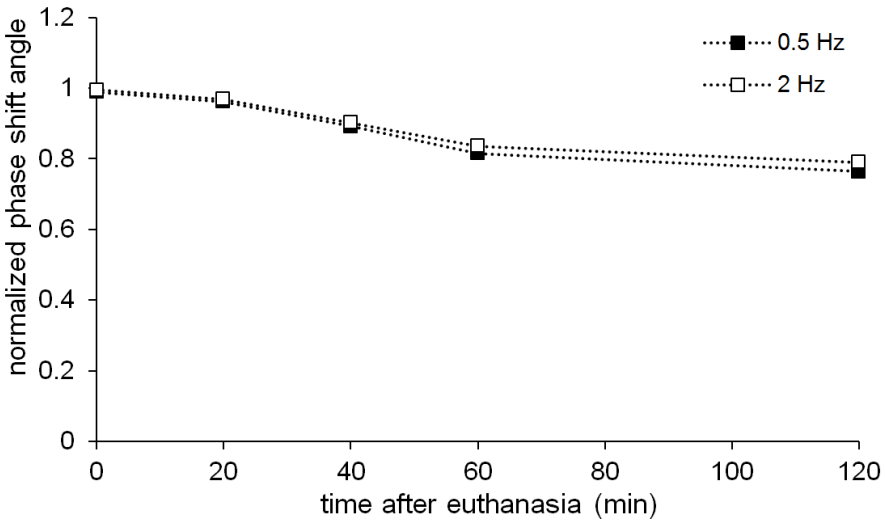

Figure 3.7. Phase shift angles of the sample configuration I as a function of time after euthanasia, normalized using the phase shift angle obtained from the anesthetized animal. The loading frequencies are 0.5 Hz and 2 Hz.

respectively (Fig. 3.8C, 3.8D). Damage to the structure of the tibia resulting from the loading regimen was not observed in any of the samples.

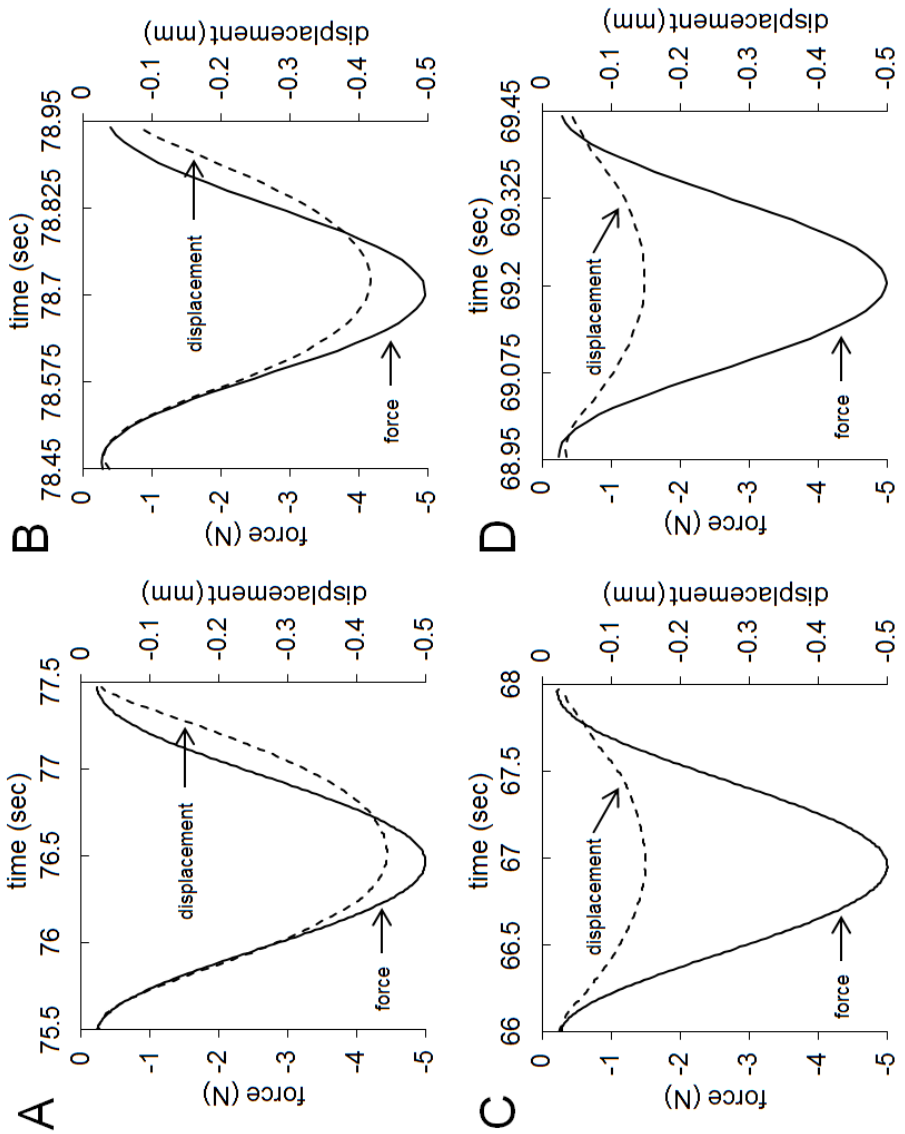

Figure 3.8. Force and displacement diagram. (A) Loading at 0.5 Hz for the sample configuration I. (B) Loading at 2 Hz for the sample configuration I. (C) Loading at 0.5 Hz for the sample configuration V. (D) Loading at 2 Hz for the sample configuration V.

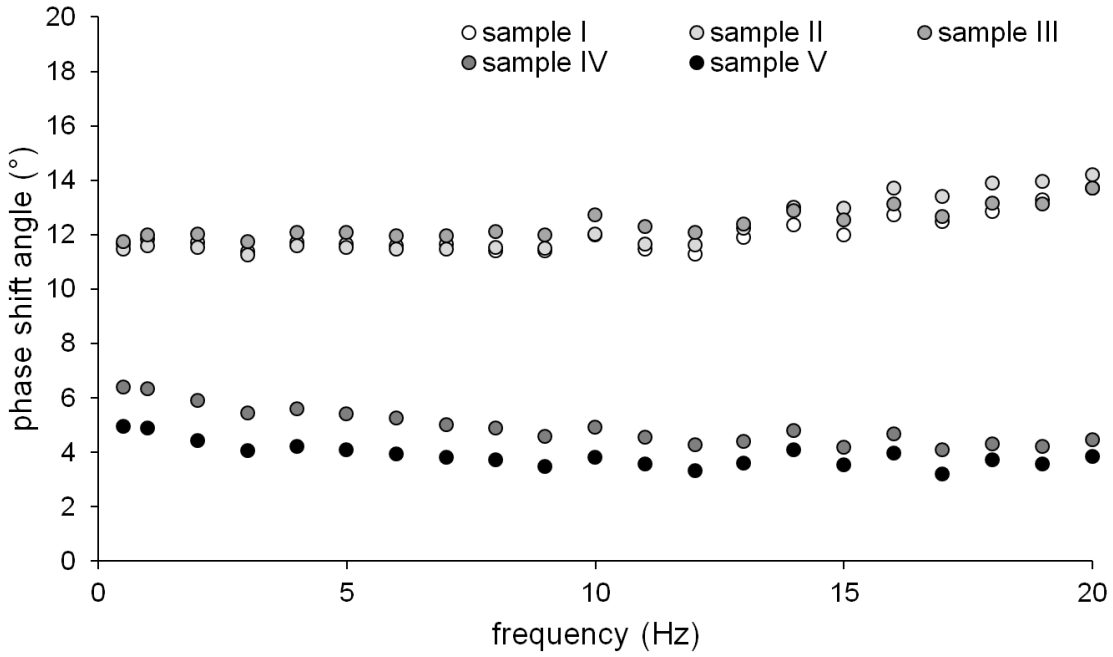

Figure 3.9. Effects of loading frequency on phase shift angle. Phase shift angles for the sample configurations I - V in response to a force waveform consisting of a series of individual sinusoidal components from 0.5 to 20 Hz.

A significant phase shift angle was observed for all sample configurations (Fig. 3.9). Note that the contribution of the loading system has been removed from the values shown. Among five configurations, phase shift angles of samples I through III tended to increase slightly with increasing frequency, and no statistical difference was seen between these samples at any frequency ($p \geq 0.38$). Sample configuration I showed an increase in phase shift angle from 11.6°at 0.5 Hz to 13.7°at 20 Hz, and samples II and III showed similar trends. Phase shift angles of samples IV and V were significantly lower than those of sample I at all frequencies, and showed very little dependence on frequency as frequency increased ($p < 0.001$). For example, sample configuration V produced a phase shift angle of 5.0°at 0.5 Hz and 3.9°at 20 Hz. The large drop in phase shift angle between sample III and IV corresponded with the removal of the knee joint, and contributed to a 45%, 50%, and 68% decrease in phase

shift angle at 0.5, 2, and 20 Hz, respectively (Fig. 3.10). The ratio between the phase shift angle of stage V (bone alone) and stage I (intact hindlimb) demonstrated the influence of the tibia alone. This ratio was 43% at 0.5 Hz, 38% at 2 Hz, and 28% at 20 Hz. Removal of the ankle, skin, and muscle exhibited the smallest effects on phase shift angle, contributing to approximately 14% of the total phase shift at each frequency.

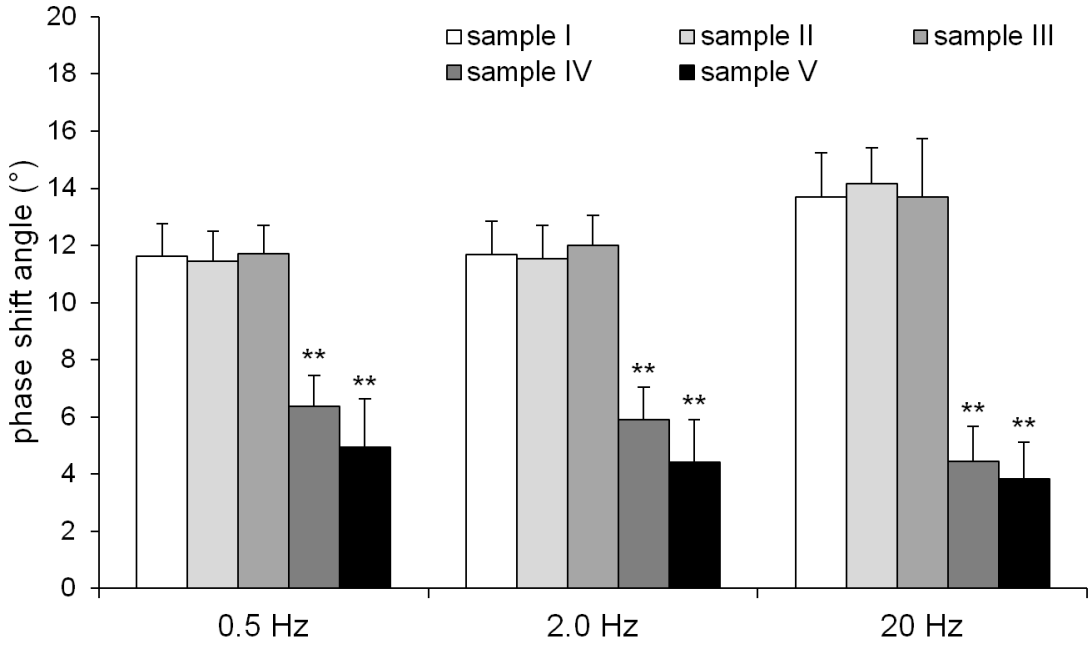

Figure 3.10. Effects of loading frequency on phase shift angle. Phase shift angles for sample configurations I - V at 0.5, 2, and 20 Hz. Significance denoted in reference to sample configuration I.

3.2.3 Determination of Dissipation Energy (Energy Loss)

In response to axial loading of hindlimb samples with a sinusoidal waveform at 0.5 Hz, the representative force-displacement relationships are illustrated (Fig. 3.11). In those plots, the areas surrounded by closed loops correspond to dissipation energy due to hysteresis. Figure 3.12 exhibits dissipation energy per cycle for the samples I - V at

0.5, 2, and 20 Hz. At 0.5 Hz, dissipation energy gradually decreased between sample I and III from 0.29 mJ to 0.25 mJ, respectively, with statistical significance seen between samples I and III ($p < 0.03$). A much steeper, statistically significant drop was found between sample I and IV in all frequency groups ($p < 0.001$). Samples IV and V showed very similar dissipation energies near 0.03 mJ per cycle. While similar trends in energy dissipation are seen in response to 2 and 20 Hz waveforms, the magnitude of the energy loss in each sample configuration decreased monotonously as the frequency was increased. The dissipation energy in sample I was 0.29 mJ at 0.5 Hz, 0.27 mJ at 2 Hz, and 0.11 mJ at 20 Hz, and in sample V decreased to 0.03 mJ at 0.5 and 2 Hz and 0.01 mJ at 20 Hz. The dissipation energy of the sample V was approximately 9% that of sample I at 0.5 and 2 Hz, and 11% at 20 Hz. Dissipation energy followed a similar trend as phase shift angle with a large decrease between sample III and sample IV. This drop, which corresponded with the removal of the knee joint, accounted for approximately 71%, 72% and 69% of the energy dissipated by the intact hindlimb at 0.5 Hz, 2 Hz, and 20 Hz, respectively. Skin was found to contribute to approximately 12% of the total dissipated energy at all frequencies, and the remaining energy was lost with removal of the muscle and foot.

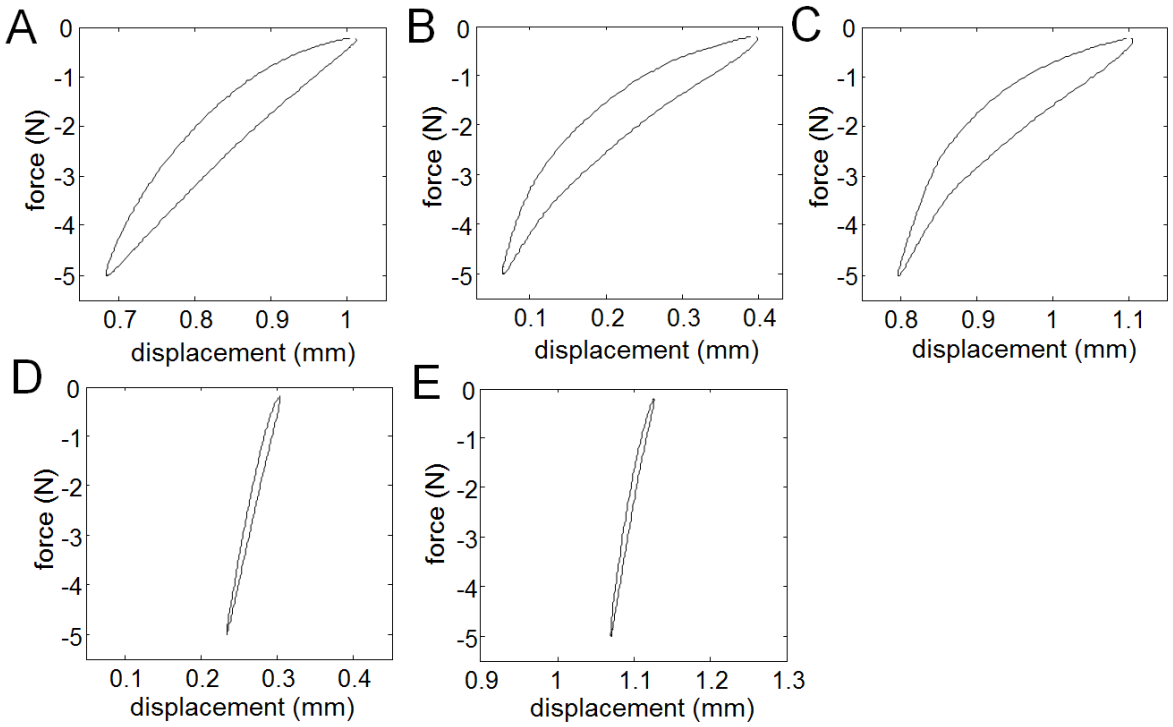

Figure 3.11. Force-displacement relationship. (A) Loading at 0.5 Hz for the sample configuration I. (B) Loading at 0.5 Hz for the sample configuration II. (C) Loading at 0.5 Hz for the sample configuration III. (D) Loading at 0.5 Hz for the sample configuration IV. (E) Loading at 0.5 Hz for the sample configuration V.

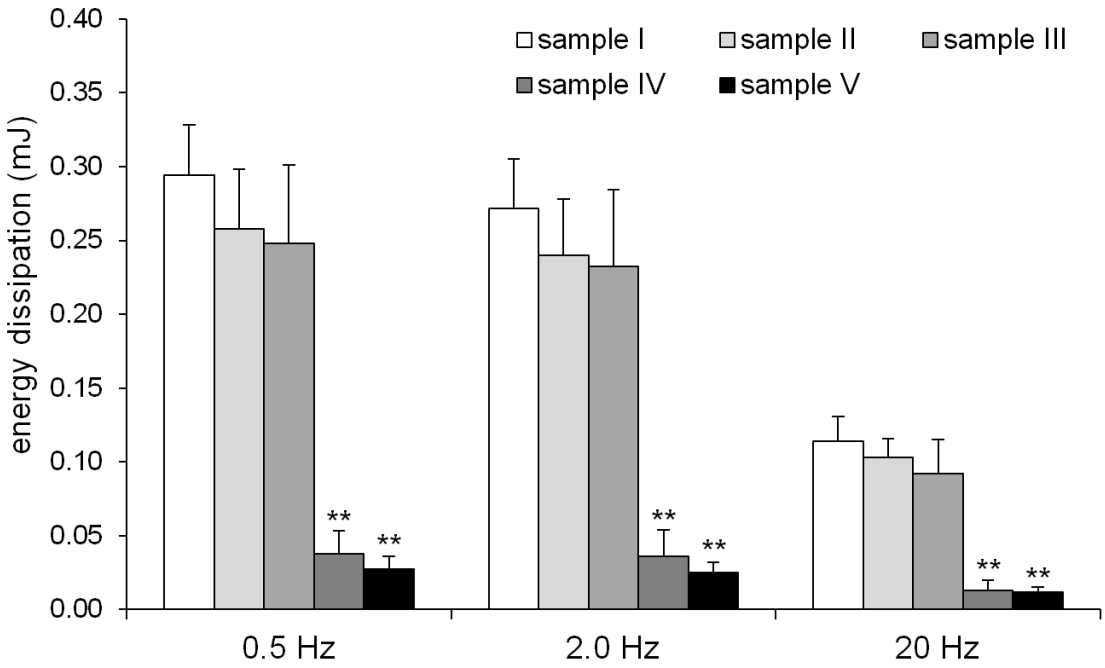

Figure 3.12. Energy loss due to hysteresis. Energy loss per cycle for the sample configurations I-V in response to loading at 0.5, 2, and 20 Hz. Significance denoted in reference to sample configuration I.

3.2.4 Bone Histomorphometric Analysis of Tibiae Exposed to Constant-Frequency Axial Bending

To evaluate a potential link between bone bending and load-driven bone formation, new bone formation resulting from axial tibia loading of three mice was investigated using histomorphometry. Consistent with the positions of bending-moment driven stress, tibia loading enhanced bone formation in the proximal and middle sections but no significant labeling was observed in the distal section (Fig. 3.13). Furthermore, the medial and lateral surfaces were more strongly labeled than the anterior and posterior surfaces.

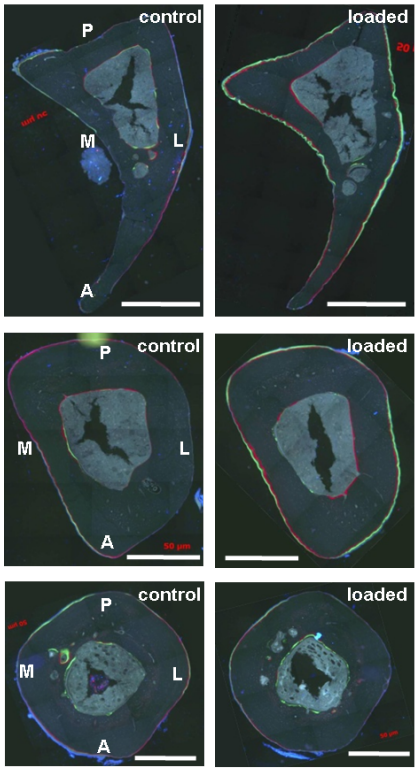

Figure 3.13. Tibia loading for bending analysis and histology. Three mice underwent constant-frequency axial tibia loading and bending-induced bone formation was analyzed using bone histomorphometry. Fluorescently double-labeled tibia cross-sections were produced at the proximal (25%), middle (50%), and distal (75%) positions. The left images are controls, and the right images tibia loading. The letter labels are: P - posterior; A - anterior; M - medial; and L - lateral. Bar = 500 μm.

3.2.5 Changes in vBMD of Tibiae Axially Loaded with Variable-Frequency Waveforms

Axial loading was subjected to the tibiae of mice at a low, medium, and high frequency range. Spectral analysis of the loading waveform in each group verified that the focus of each signal was applied to the intended frequency range in each loading group (Fig. 3.3B).

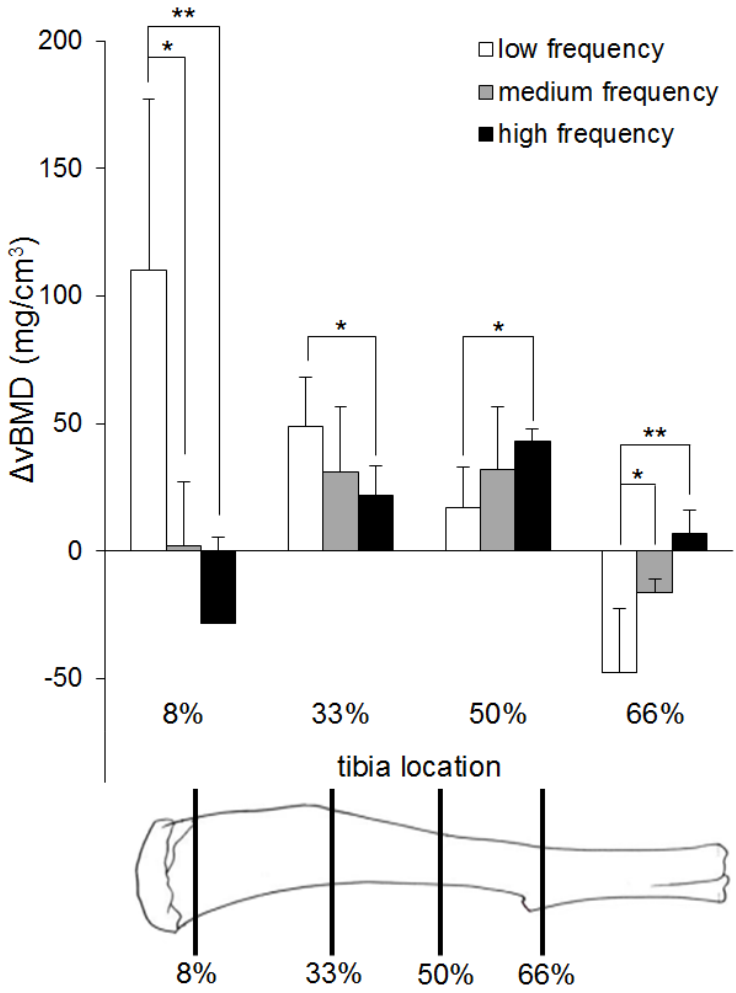

Figure 3.14. Difference in vBMD was determined between non-loaded and loaded samples at 8%, 33%, 50%, and 66% of the tibia's length. Medium and high frequency responses were compared to the low frequency response using a two-tailed Student's t-test to determine statistical significance.

Volumetric BMD was used to quantify bone formation in the loaded samples (Fig. 3.14). Difference in vBMD ($\Delta vBMD$) was defined as the average vBMD of contralateral control (left tibiae) samples subtracted from the average vBMD of the loaded samples (right tibiae). Little change in vBMD was seen at the 8% location in samples loaded with a medium frequency waveform. However, an increase in vBMD of 109.9 mg/cm^3 in the low frequency group and a decrease in vBMD of 28.5 mg/cm^3 in the

high frequency group were seen at this tibia location, a statistically significant difference ($p < 0.01$). At the 33% mark, increases in vBMD of 48.6 mg/cm^3, 31.0 mg/cm^3, and 21.6 mg/cm^3 in response to low, medium, and high frequency waveforms, respectively, were observed. In the distal section of the bone, the trend of larger vBMD gains in the low frequency group that was seen in the 8% through 33% tibia locations was reversed. A small increase in vBMD due to a low frequency waveform at the 50% location was seen, but a statistically larger increase of 42.9 mg/cm^3 was noted in the high frequency group ($p < 0.05$). At the 66% location, a decrease in vBMD of approximately 47.6 mg/cm^3 was observed in the low frequency group, while a small, but significantly different increase in vBMD was noted in response to a high frequency waveform ($p < 0.01$).

3.2.6 Bone Histomorphometric Analysis of Tibiae Exposed to Variable-Frequency Stimulation

To distinguish the exact locations of observed bone formation in loaded samples, bone histomorphometry was utilized using calcein and alizarin labeling. Non-loaded control samples, in addition to low and high frequency loaded samples, were analyzed at 8% and 66% of the tibia's length. Representative histomorphometric sections demonstrate that low and high frequency provided maximum bone stimulation in the 8% and 66% locations, respectively, when compared to a non-loaded contralateral control (Fig. 3.15). Specifically, low frequency loading was found to produce the largest enhancement of bone formation in the medial quadrants of the 8% cross section, while a smaller degree of stimulation was observed in the posterior-lateral quadrant of the 66% cross section. Most bone formation was noted on the periosteum in each low frequency-loaded section. High frequency loading provided maximum stimulation in the periosteal posterior-medial and anterior-lateral quadrants of the 66% cross section, and some stimulation was also noted in posterior portions of the endosteum.

The 8% cross section, while experiencing less bone formation than the 66% section, showed maximum stimulation on the anterior face of the periosteum and sections of the posterior-lateral quadrant of the endosteum.

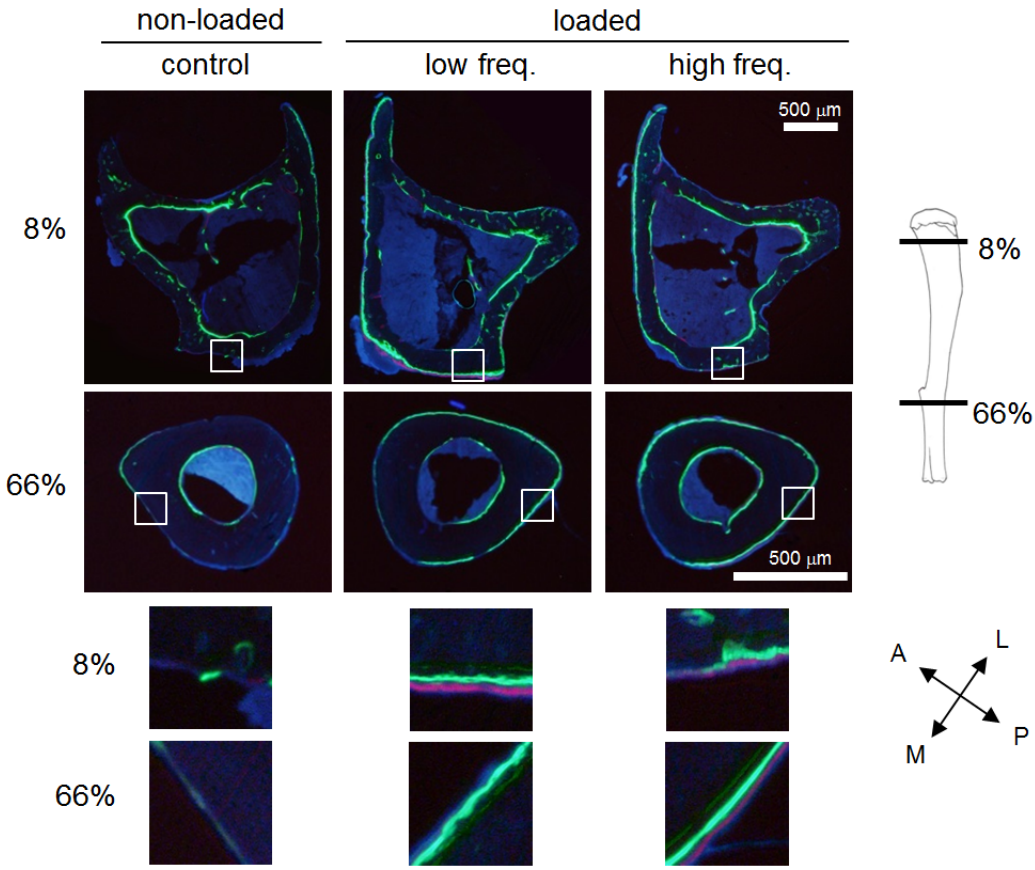

Figure 3.15. Bone histomorphometry. Representative histomorphometric images of the 8% and 66% cross sections. Calcein (green) and alizarin (red) labeling was used to visualize areas of maximum bone formation in response to no loading, low frequency loading, and high frequency loading. Inset boxes demonstrate representative regions of interest.

Percent change in LS/BS was determined to quantify the observed frequency dependence in bone formation. In the proximal tibia (8% length) the percent increase in LS/BS was 20.9% in samples loaded at a low frequency, and 9.6% in samples loaded at a high frequency, a statistically significant difference ($p < 0.01$) (Fig. 3.16). At

66% of the bone's length, the increase in LS/BS in loaded samples was 18.6% and 25.8% at low and high frequencies, respectively. A statistically significant increase in percent change in LS/BS was found between samples subjected to a high frequency load at 8% and 66% of the tibia length ($p < 0.01$).

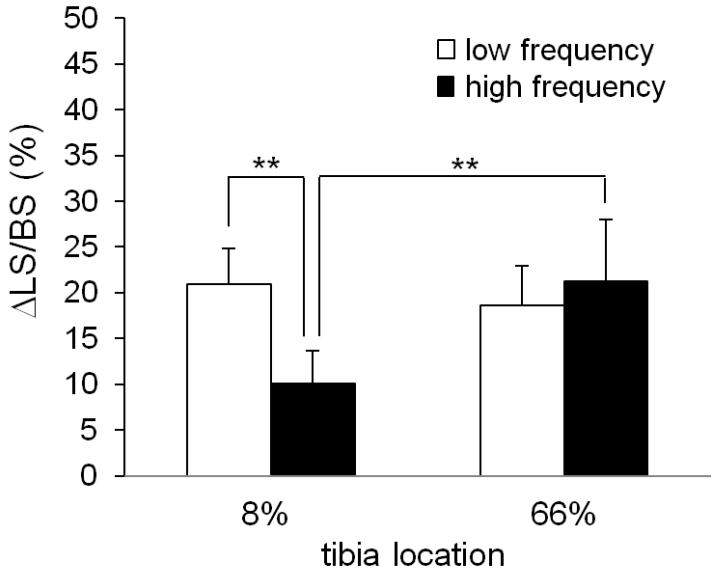

Figure 3.16. The change in ratio of labeled surface to bone surface (ΔLS/BS) was determined at the 8% and 66% locations in response to low and high frequency loading waveforms. Statistical significance was determined between the low and high frequency response at the 8% location and the high frequency responses at each location using a two-tailed Student's t-test.

3.2.7 FE Analysis of Curvature in the Mouse Tibia

Phase shift angles in response to 0.5, 2, and 20 Hz sinusoidal waveforms were compared for each the model derived from μCT images as well as for the models created to test the effects of curvature on damping. Using the μCT model, phase shift angles of 4.14°, 4.06°, and 4.09°were determined in response to force waveforms at 0.5, 2, and 20 Hz, respectively. Using the same material properties and radius

of curvature, the secondary model predicted phase shift angles of 4.26°, 4.16°, and 4.41°at 0.5, 2, and 20 Hz, a difference of 2.8%, 2.4%, and 7.3%, respectively.

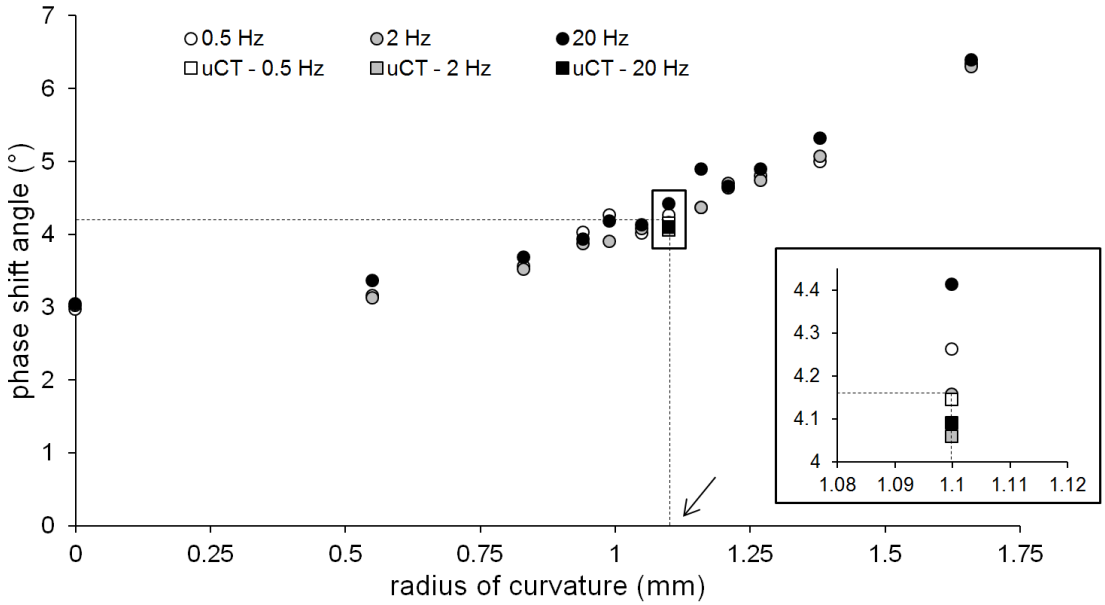

Figure 3.17. FE prediction of phase shift angle. FE models were subjected to sinusoidal force waveforms at 0.5, 2, and 20 Hz. Prediction of the phase shift angles as a function of the maximum radius of curvature of the tibia. The dotted lines pinpoint the location of the physiologically normal model, with the arrow corresponding to 1.1 mm. Inset rectangle shows a zoomed view of the area surrounded by a box.

The radius of curvature was altered from the physiological value in a range of 0 to 1.66 mm, or 0 to 150% of the normal value to simulate the effects of curvature on phase shift angle (Fig. 3.17). For $d = 0$ mm (0% of normal), the phase shift angle was predicted to be 2.97°at 0.5 Hz, 3.02°at 2 Hz, and 3.04°at 20 Hz. These predicted phase shift angles were 44%, 38%, and 45% lower than those for a tibia with normal curvature at 0.5, 2, and 20 Hz, respectively. As the radius of curvature was changed to 0.83 mm (75% of normal), the predicted phase shift angle increased slightly to 3.56°, 3.51°, and 3.68°at 0.5, 2, and 20 Hz, respectively. As the radius of curvature further increased, the rate of increase of the phase shift angle was predicted to accelerate.

At $d = 1.38$ mm, or 125% of normal, the phase shift angle was predicted to be 4.99°, 5.07°, and 5.32°at 0.5, 2, and 20 Hz, respectively. Finally, at $d = 1.66$ mm (150% of normal), the predicted phase shift angle was 6.34°at 0.5 Hz, 6.30°at 2 Hz, and 6.39°at 20 Hz. In this highly-curved case, the predicted phase shift angles were 49%, 52%, and 45% higher than those for a normal tibia at 0.5, 2, and 20 Hz, respectively.

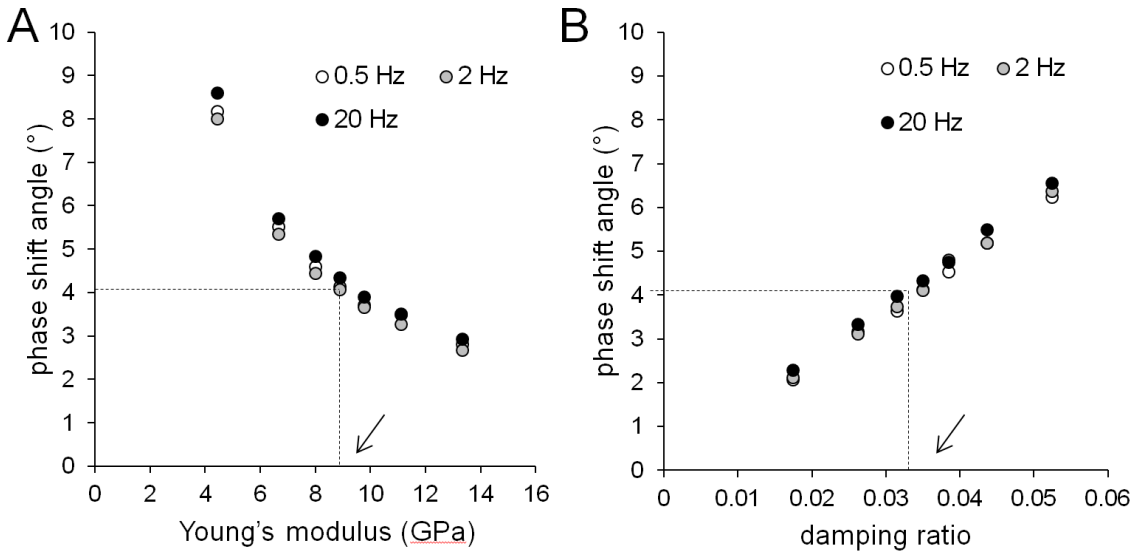

Figure 3.18. (A) Sensitivity analysis showing the predicted phase shift angles when the elastic modulus of the model is altered. The dotted lines demonstrate the location of the physiologically normal model, with the arrow corresponding to 8.9 GPa. (B) Sensitivity analysis showing the predicted phase shift angles when the damping ratio of the model is altered. The dotted lines show the location of the physiologically normal model, with the arrow corresponding to 0.035.

To evaluate the effects of certain material properties on the phase shift angle predicted by the model, sensitivity analysis simulations were conducted for the Young's modulus and damping ratio (Fig 3.18). Each variable was altered to between 50 and 150% of the value obtained from literature, while the radius of curvature and all other properties were held constant at their normal values. As Young's modulus increased, the FE model predicted that the phase shift angle would decrease at a decaying rate.

As damping ratio increased, the model predicted that phase shift angle would increase linearly.

3.2.8 Determination of Resonant Frequencies and Modes

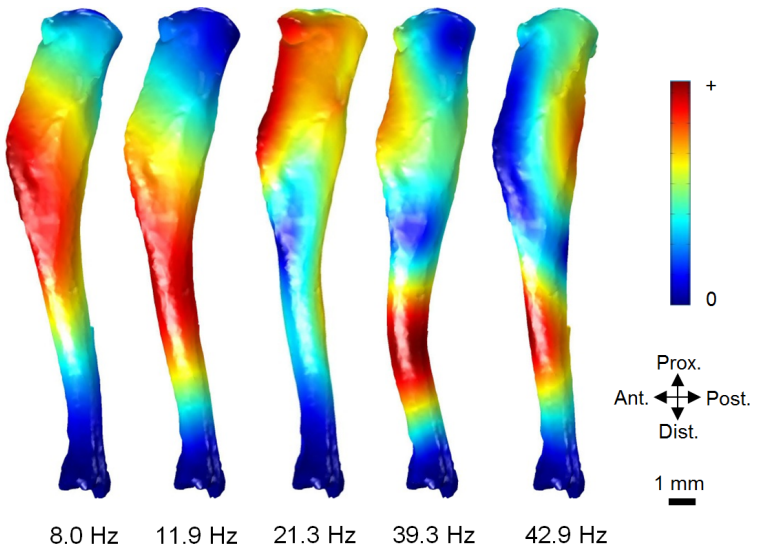

Figure 3.19. Modal analysis using FE methods to determine the resonant frequencies and modes of vibration of the tibia. The first five resonant frequencies were determined to be 8.0 Hz, 11.9 Hz, 21.3 Hz, 39.3 Hz, and 42.9 Hz. Displacement distributions demonstrate areas of maximum motion during vibration, where red zones denote larger displacements.

Modal analysis using FE modeling was utilized to determine the first five resonant frequencies and vibrational modes of a tibia model. These frequencies were found at 8.0 Hz, 11.9 Hz, 21.3 Hz, 39.3 Hz, and 42.9 Hz for modes 1 through 5, respectively. Displacement distributions were modeled in order to obtain a visualization of the movement experienced by the tibia during vibration at each frequency (Fig. 3.19). Red colors demonstrate areas subjected to a higher peak displacement, while blue colors showed displacements near zero. The mode of vibration corresponding to the

first two frequencies exhibited bending across the entire bone, where peak displacement is found near the 33% distal mark in mode 1 and the midshaft in mode 2. Peak displacements in Modes 3 through 5 provide evidence of more than one axis of bending. For example, modes 4 and 5 showed small displacements near the proximal end, but larger movement was seen near the 66% distal mark.

3.2.9 Principal Strain Analysis of Vibration at Resonant Modes

FE analysis was used to demonstrate the distributions of first principal strains during vibration at the first five resonant frequencies (Fig. 3.20). Blue colors designate locations predicted to experience strains close to zero, while red areas are predicted to experience larger positive (tensile) strains. The first two modes, vibrating at a frequency of 8.0 Hz and 11.9 Hz, were subjected to the highest levels of first principal strains near the proximal end, with slightly smaller values seen near the midshaft and distal end. The third mode, which vibrates at 21.3 Hz, saw peak first principal strains near the midshaft and 66% mark. The fourth and fifth modes (39.3 and 42.9 Hz, respectively) each showed peak first principal strain values near the 50% and 66% marks, with lower values demonstrated proximally. Each mode showed a small region of higher strain near the distal end of the bone beyond the 66% mark. Cross sections at the 8% and 66% locations demonstrate first principal strain distributions within the cortical bone for each of the first five modes (Fig. 3.21). The first through third modes were predicted to experience the largest areas of high first principal strain at the 8% location, primarily in the posterior-lateral quadrant. The fourth and fifth modes experienced lower magnitude strains at this location. In the 66% location cross section, the predicted position of peak first principal strain varied between vibrational modes, but the second through fifth modes were expected to experience the highest magnitude strain.

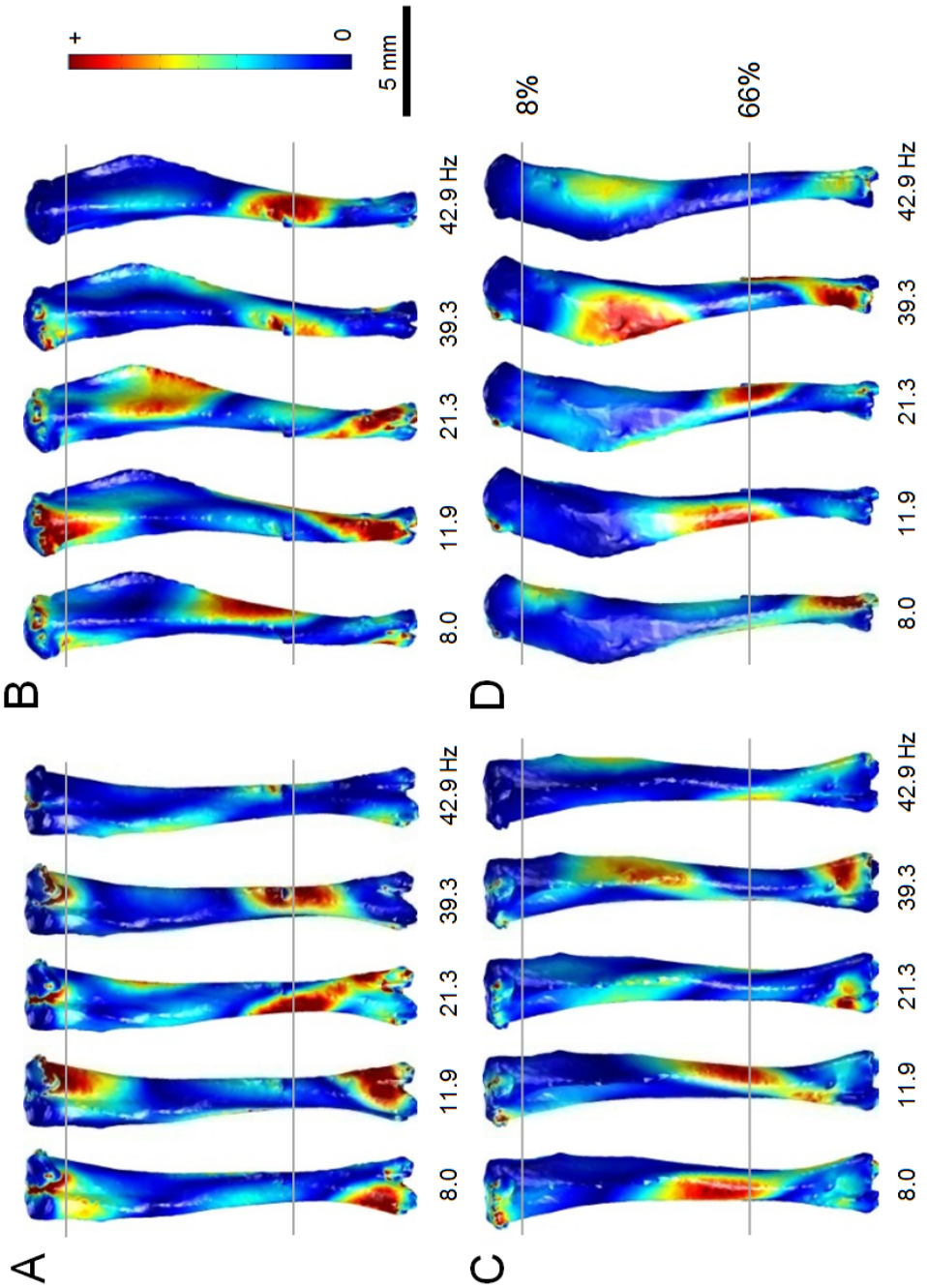

Figure 3.20. Distribution of first principal strains in the first five vibration modes of the tibia. Red coloring represents areas of greater positive (tensile) strains, while blue coloring denotes areas experiencing very little strain. (A) Posterior surface. (B) Lateral surface. (C) Anterior surface. (D) Medial surface.

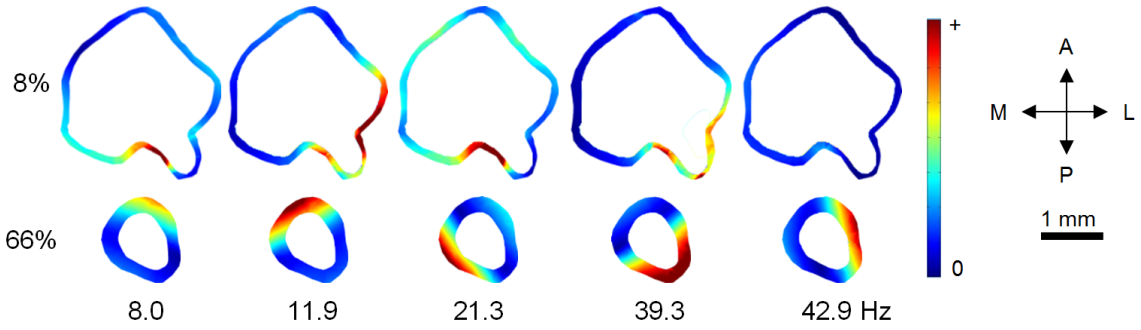

Figure 3.21. Distribution of first principal strains from the first (8.0 Hz) and fifth (42.9 Hz) modes were analyzed within the 8%, 33%, 50%, and 66% cross sections.

The third principal strain distributions in the first five vibration modes of the tibia were also studied using FE analysis (Fig. 3.22). Red colors represent areas that were predicted to undergo negative (compressive) third principal strains, while blue colors denote locations where strains are near zero. In the first two vibrational modes predicted by the FE model, peak third principal strains were in the ends and midshaft of the tibia, with very little strain near the 33% mark. The third, fourth, and fifth modes were predicted to show smaller magnitudes of third principal strain in the proximal end of the bone, but larger magnitude strains in the 33% to 66% marks. In the fourth and fifth modes, the peak second principal strain was predicted near the 66% location, but significant strains were also found near the 33% mark. Cross sections demonstrate third principal strain distributions in the cortical bone at 8% and 66% locations (Fig. 3.23). Peak third principal strains were predicted in the anterior-lateral quadrant of the 8% location in the first vibrational mode. The second through fifth modes were expected to experience lower magnitude strains. At the 66% location, the maximum strains were expected in the posterior-medial quadrant of the higher modes, with the lower modes showing smaller magnitudes of strain.

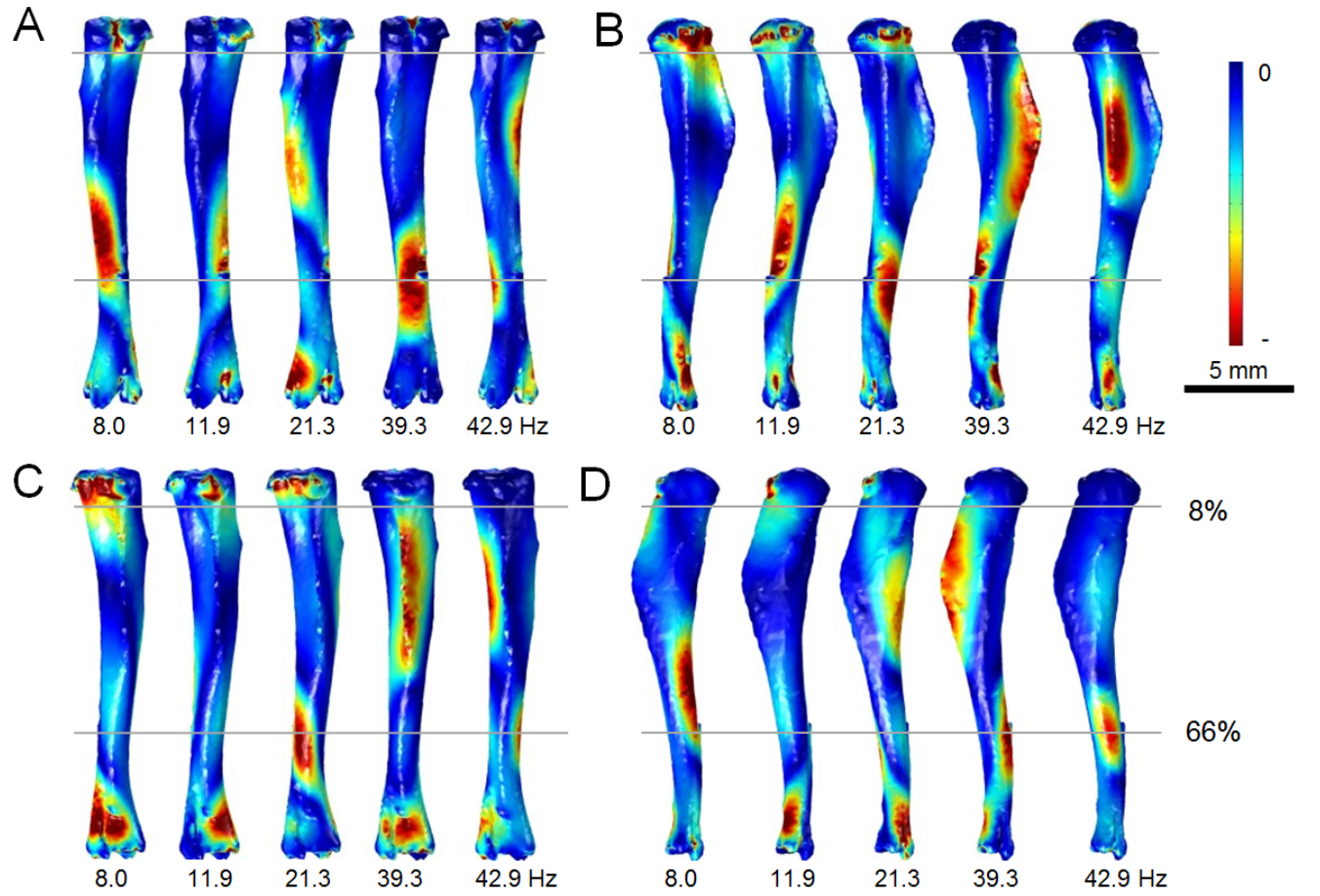

Figure 3.22. FE analysis of third principal strains in the first five vibration modes of the tibia. Red coloring represents areas of greatest compressive strains, while blue coloring denotes areas experiencing strain near zero. (A) Posterior surface. (B) Lateral surface. (C) Anterior surface. (D) Medial surface.

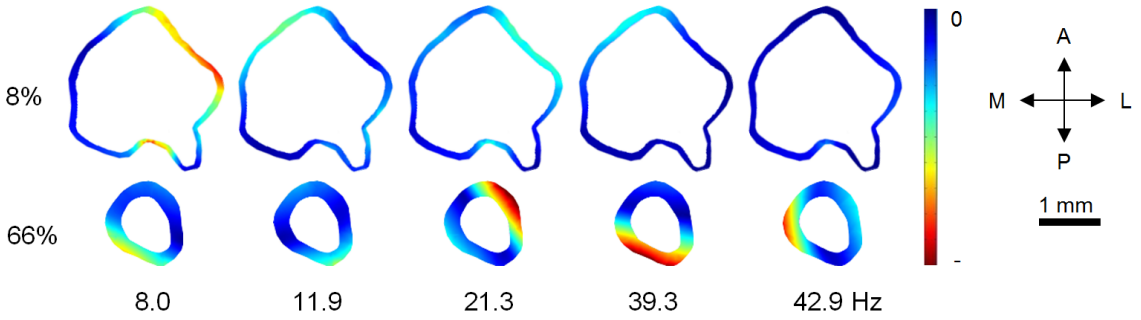

Figure 3.23. Distribution of third principal strains from the first (8.0 Hz) and fifth (42.9 Hz) modes were analyzed within the 8%, 33%, 50%, and 66% cross sections.

The relative principal strain at the 8% location to the 66% location was calculated for each of the vibrational modes to quantify locations of maximum first and third principal strains (Fig. 3.24). Predicted strains in the 8% section were approximately 20% and 30% greater than strains predicted in the 66% section of the lowest mode for the first and third principal strain, respectively. The ratio dropped to approximately one in the second mode for each the first and third principal strains, and continued to fall consecutively in the third through fifth modes. In the third and fourth modes, the expected first and third principal strains at the 8% location were approximately 40% to 60% of those at the 66% location. In the fifth mode, strains at the 66% location were predicted to be approximately 4-fold larger than at the 8% location for each the first and third modes.

3.3 Discussion

The *ex-vivo* experimental data demonstrated that mouse lower hindlimbs exhibited substantial viscoelastic characteristic, and depending on the sample configurations and loading frequency dynamic loading induced 4 - 14˚phase shift angles and

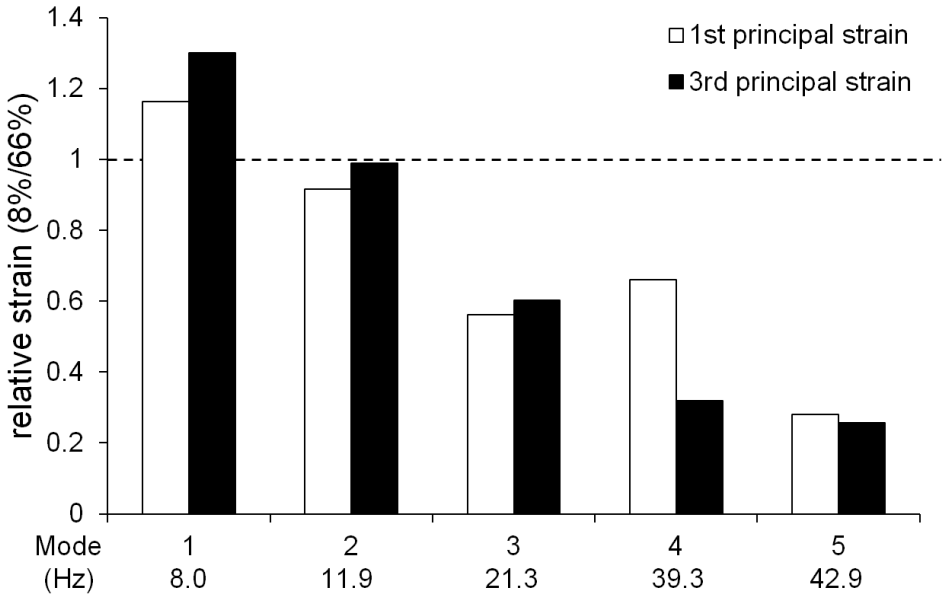

Figure 3.24. Relative strain between 8% and 66% locations in the first five vibrational modes of the tibia. First and third principal strain values at each node of the FE mesh in the 8% and 66% cross sections were summed then divided by the total number of nodes. Data shown represents a ratio of the average strain at the 8% location to that of the 66% location for each vibrational mode.

0.01 – 0.3 mJ energy loss per cycle. The maximum damping capacity was obtained for the intact lower hindlimb without any tissue removal. Interestingly, bone alone significantly contributed to the damping capacity, with approximately 43% of the total phase shift angle attributed to bone in response to loading at 0.5 Hz, declining as frequency increased to 28% at 20 Hz. Energy dissipated in the bone was found to be between 9 and 11% of that of the intact limb at all frequencies.

Most of the remaining portion of the damping capacity of the lower hindlimb was a result of the knee joint and muscle tissue surrounding the bone, with the skin and ankle joint adding very little influence. The small contribution of the ankle joint might be a result of the boundary conditions of the experimental setup, as both the ankle in

sample configuration II and the distal end of the tibia in sample configuration III were potted in the base of the loader. The knee joint alone accounted for approximately 45 - 58% of the total phase shift angle, and approximately 69 - 72% of the dissipated energy, depending on frequency. This result suggests that the knee joint, in addition to bone, plays a significant role in the damping capacity of the hindlimb.

The *in-vivo* experimental data demonstrated a dependence of the maximum bone formation on location and frequency of loading. Samples loaded with the low frequency waveform exhibited peak enhancement of bone formation in the proximal (8-33%) locations of the tibia, while the high frequency waveform offered the greatest enhancement in the midshaft (50%) and distal (66%) sections. In the midshaft and distal sections, this trend was reversed, and largest increases in bone formation were observed when a high frequency load was applied. These results suggest that the proximal section responds most strongly to low frequency loading (1-17 Hz), while medium (18-34 Hz) and high (35-51 Hz) frequency loading provide successively diminished beneficial effects. The midshaft and distal sections respond strongest to high frequency loads, with low and medium frequency loads providing a smaller anabolic effect.

FE analysis predicted that curvature has a significant impact on the damping capacity of the tibia. Phase shift angles produced in a normal tibia model ($d = 1.1$ mm) were predicted to be 4.26°at 0.5 Hz, 4.16°at 2 Hz, and 4.41°at 20 Hz. When the radius of curvature was reduced to zero, simulating a straight bone, the phase shift angle decreased to approximately 3°at all frequencies. This result suggests that bending due to natural curvature accounts for approximately 38 - 45% of the total damping capacity of a normal tibia depending on frequency, with the remaining portion due to internal compressive properties. As the radius of curvature of the tibia model was increased to 1.66 mm, simulating a highly-curved bone, phase shift angles were predicted to increase by approximately 45 - 52% (depending on frequency) when

compared to a tibia of natural curvature, or approximately 110% when compared to a zero-curvature model. This result indicates that increased curvature non-linearly enhances mechanical damping in the tibia.

Histomorphometric analysis of tibiae loaded with a constant-frequency waveform supports the notion that bone curvature enhances load-driven bone formation on the periosteal surface in a position dependent manner. FE analysis predicted that the first vibration mode depicted in Fig. 3.19. This mode with the resonance frequency at 8.0 Hz is mainly caused by bone curvature in the proximal half of the tibia and it significantly deforms the proximal and middle portions without deforming the distal portion. The bending motion is predicted along the mediolateral direction, which is consistent with enhanced fluorescent signals on the medial and lateral surfaces of the proximal and middle transverse sections. The frequency for tibia loading in this study was 2 Hz, and the first vibration mode was lowest and closest to the loading frequency. Other vibration modes at higher frequencies present different bending patterns and the FE and histological results suggest that bone curvature is involved in its load-driven bone formation in a frequency and position dependent fashion. Collectively, bone curvature contributes to not only mechanical damping in bone but also load-driven bone formation.

Evolution of the geometric shape of bones is thought to be determined by a variety of environmental factors. For example, the shape of the human femur is thought to be impacted by climate adaptation [86]. Therefore, it is conceivable that temperature may also be a factor in the shape of the tibia. Other studies have proposed that bone shape is affected by loading during activity. For example, it has been suggested that the consistency of bending-induced strain patterns developed in long bones during physical activity may explain why curvature is a desirable structural aspect [87]. Furthermore, it has been proposed that the curved shape of long bones, while reducing overall axial strength, increases predictability and better distributes

stresses within the bone during loading [88]. Curvature has also been identified as an important modulator of bone stiffness during development [89]. Of the bone configurations considered in this study, the greatest axial strength corresponded to a perfectly columnar tibia with no curvature ($d = 0$ mm). This configuration, however, was found to significantly decrease the damping capacity of the bone and reduces bending motion. The configuration corresponding to the largest damping capacity and bending motion was a highly-curved shape ($d = 1.66$ mm); however, this shape reduced axial strength. Collectively, the results of this study suggest that the appropriate amount of bone curvature may enhance shock-absorbing dampening effects and stimulate bone remodeling, but excessive curvature may induce detrimental effects.

Modal analysis using FE modeling provided a correlation between the *in-vivo* experimental results and the vibrational modes. The first five resonant frequencies were predicted to be 8.0, 11.9, 21.3, 39.3, and 42.9 Hz, and distributions of first and third principal strains were determined. The average first and third principal strains at the 8% mark were predicted to be at least 20% greater than strains at the 66% mark in the first vibrational mode, and approximately 4-fold less in the fifth mode. Since areas of higher first and third principal strains are expected to exhibit more bone formation, a link to experimental data was detected. FE predictions show that mechanical loading in the range of the lower frequency group, corresponding to the frequencies of vibration of the first two resonant modes, should provide maximum enhancement of bone formation in the proximal tibia. Higher frequency loading, which encompasses the fourth and fifth predicted resonant modes, is expected to provide the greatest enhancement of bone formation in the midshaft and distal sections of the bone.

FE analysis also provided a correlation between predicted principal strains and maximum bone formation within the 8% and 66% cross sections. In the 66% cross section, for instance, peak third principal strain was predicted in the posterior-medial

quadrant, approximately the same area that experienced the most bone growth following high frequency loading. Peak first principal strain was predicted in the anterior-lateral quadrant, an area that also experienced bone growth in response to high frequency loading. While correlations were not as strong in the 8% cross section, a link between bone formation due to low frequency loading in the medial quadrants and principal strains predicted in the proximal-medial quadrant of the first mode was observed. The weaker correlation at the 8% level may be due to small variations in geometry between the bone used for the representative histomorphometry section and the bone used to construct the FE model. These variations may alter strain distributions and resulting bone formation.

When a periodic load is applied at or near one of an object's resonant frequencies, it tends to absorb more energy and oscillate at greater amplitudes than at other loading frequencies. In the case of the tibia, loading at frequencies near the resonant frequencies of the bone may be causing more energy to be dissipated and larger displacements in certain areas of the bone than loading at other frequencies with equal amounts of force. This may lead to increased strain rates, amplified intramedullary fluid flow, increased fluid shear stresses on bone cells, and enhanced cellular response in areas that absorb the most energy [44, 58, 90]. Compressive strain on the medial face of the midshaft of the tibia due to a 7 N axial load at 2 Hz has been shown to be approximately 1,250 $\mu\epsilon$ [50, 51]. In addition to resonance, other factors likely contribute to the observed frequency dependence of maximum bone formation. For example, bone is a vascularized organ with a network of neurons. Mechanical loading is known to affect blood circulation as well as neuronal signaling [91, 92]. Therefore, loading-induced bone formation cannot be attributed solely to biomechanical factors.

Because of the effects of damping in surrounding tissues, it is expected that transmission of the loading force through surrounding tissues, such as skin, muscle, and joint tissue, may modify the frequencies at which the tibia resonates [73, 93, 94]. In

addition, frequencies of vibration may vary among individual animals based on slight alterations in size or proportion. To allow for potential variations in actual resonant frequencies, a composite loading waveform was developed. This waveform allowed for many frequencies of loading to be applied in a single loading session in each a low, medium, and high frequency range, increasing the likelihood of loading near a resonant frequency.

In a simple phase shift model such as a Voigt model, a quasi-proportional relationship is predicted between a phase shift angle and energy loss. However, in our experiments, phase shift angle and dissipation energy produced varied estimations of the contribution of bone to the damping capacity of the lower limb. The most likely cause of these differences involves nonlinear viscoelastic properties of bone [72, 95]. These properties became evident when loading was applied to the bone. The displacement of bone was shown to exhibit an asymmetrical pattern in response to a sinusoidal load. As a compressive force was applied to the bone, the phase shift angle between the load and displacement was very small. However, during decompression, the phase shift angle increased as the recovery of the bone lagged behind the removal of force. Due to the varying phase shift, the least mean-square method used in data fitting may have overestimated the phase shift angle between the force and displacement in all sample configurations.

Hysteresis curves were also affected by the asymmetrical phenomenon. Unlike the compression portion of the hysteresis curve, the part of the curve corresponding to decompression to the preloaded state does not follow a path consistent with what is expected from simple viscoelastic models. Instead, non-linear viscoelastic properties cause the decompression curve to mirror the compression curve, forming a crescent-shaped hysteresis loop. This phenomenon leads to a lower energy loss than might be expected in all sample configurations.

The current study has limitations in the *ex-vivo* and *in-vivo* experimental setups and computational simulations. First, in the *ex-vivo* tibia loading experiment, loading conditions were employed with 5 N (peak-to-peak) force in a sinusoidal wave, and loading was applied to euthanized animals. Differences in a phase shift angle between the anesthetized and euthanized animals were approximately 4% when the experiment was conducted within 20 min after euthanasia. Damping of bone and surrounding tissues is dependent on the loading and tissue conditions, and data in this study needs to be interpreted under these experimental conditions. Second, the FE analysis focused only on the tibia, excluding effects of the surrounding soft tissues and the fibula. A more comprehensive three-dimensional model could be developed to investigate damping in all surrounding soft tissues. Third, intramedullary fluid in a bone cavity is reported to move in response to mechanical loading and thus its effect on damping should be evaluated [19, 96].

The *in-vivo* tibia loading experiment has limitations in the experimental data and the computational results. First, bone formation was analyzed at six positions using X-ray imaging and two positions using histomorphometry. In addition, only LS/BS was analyzed using histomorphometry, and other parameters, such as bone formation rate and mineral apposition rate could have been calculated in a more comprehensive study. Also, a more detailed scanning technique, such as μCT, could have been used to evaluate changes in BMD due to loading at different frequencies. A more comprehensive study could provide a better comparison between the experimental and computational results. Second, although cortical bone is a major structural component of the tibia and sensitive to load-driven bone formation [50,51], the overall frequency response cannot be solely attributed to cortical bone. Future studies may incorporate not only cortical bone but also trabecular bone and growth plates, as well as surrounding tissues such as muscle, skin, and joints. Third, experimental evaluation of the resonant frequencies can be conducted using a vibration table that is capable of sensing a transfer of resonance energy. For the resonance frequencies of

the mouse femur, the reported difference between the predicted and experimentally determined values was approximately 15% for the lowest frequency at approximately 20 Hz [97].

Mechanical properties of bone, such as Young's modulus, may vary depending on global factors, such as age and gender, in addition to local factors caused by anisotropy in the bone structure. For this reason, the sensitivity of the FE model to variations in Young's modulus was determined. An increase in Young's modulus of 10% was found to raise the resonant frequency of the first mode 4.9%, while a decrease in Young's modulus of 10% dropped the first resonant frequency 5.1%. This represents a non-linear relationship that is more sensitive to lower values of Young's modulus.

3.4 Conclusions

Results of this study demonstrate that curvature in the tibia significantly increases its damping capacity and leads to enhanced bone formation through bending. In addition, results show that localized enhancement of bending motions during vibration at the resonant frequencies of the tibia may enhance stimulatory effects in areas that experience high principal strain during vibration. To our knowledge, this is the first study to investigate the link between an observed frequency dependence of bending-induced bone formation due to mechanical loading and mechanical resonance of the loaded bone. In this study we employed a mouse tibia as a model system, but resonance frequencies of human bones differ [77,98]. Further investigation of the observed effects of resonance may lead to the prescribing of personalized mechanical loading treatments for patients afflicted with low bone mass.

4. CONCLUSIONS AND FUTURE STUDIES

Using *in-vivo* animal experiments, mechanical loading was shown to increase the BMD and Young's modulus of osteoporotic bone in hindlimb-suspended and OVX models of disuse and post-menopausal osteoporosis, respectively. In addition, results show that the effects of loading may not only be localized to nearby bones, but may have remote impacts in the spine. Since increases in Young's modulus and BMD may represent improvements in both the quality and quantity of bone [2], this result shows that mechanical loading may be an effective treatment for osteoporotic conditions that avoids harmful side effects common in other treatment methods.

Ex-vivo and *in-silico* biomechanical analyses of loading-induced bone formation demonstrated that bone contributes significantly to damping of forces in the hindlimb, and curvature in the geometry of the bone is a primary determinant of damping capacity. In addition, curvature was shown to lead to bending-induced bone formation near the bending axis of the bone in axial loading. Curvature, while structurally reducing the buckling strength of the bone, is apparently favored by evolution, and increases quality characteristics along with helping to initialize bone remodeling. Evidence linking resonance to local enhancements in bending-induced bone formation was also discovered using an *in-vivo* experiment and verified using FE analysis. These results further the knowledge of the biomechanical properties of bone under dynamic load, and open doors to personalized treatments for osteoporotic conditions using mechanical loading.

Since the resonant properties of a bone are not dependent on the orientation of an applied load, it is expected that similar results would be observed if knee loading was

used instead of axial loading. The vibrational modes are an inherent property based on the shape and material composing the bone, and tendencies to vibrate at certain frequencies with specific principal strain distributions at each mode would be expected regardless of type of mechanical stimulation used to initiate vibrations. These results would suggest that the loading frequency is the important aspect. However, since joint loading shows more desirable characteristics than axial loading, such as increased ease of use and lower peak loads needed for similar responses, this may be a better solution in the future. Therefore, a future study may involve repeating the *in-vivo* experiment using knee loading and verifying the results obtained using axial loading.

While this study primarily investigated the larger-scale impacts of mechanical loading on bone density and quality, future studies may examine molecular-scale contributors. The use of a molecular analysis tool, such as fluorescence resonance energy transfer (FRET) microscopy [99], may allow the determination of site-dependent activation of key bone remodeling genes, such as ras homolog member A (RhoA), validating the macro-scale results presented in this study.

Collectively, the results presented in this thesis demonstrate the powerful therapeutic potential that dynamic mechanical loading may have in the treatment of osteoporotic conditions. By using non-invasive radiography scans, such as CT or magnetic resonance imaging (MRI), detailed computational models of a patient's skeleton may easily be constructed and resonance characteristics determined. Application of mechanical loading at an exact frequency to stimulate site-specific bending strains could be used to develop personalized treatments targeting bone formation to localized areas. For example, MRI images of an osteoporotic patient's femur could be used to build a FE model, and the frequency of loading to best stimulate bone formation in a problematic areas, such as the femoral neck, could be determined. A loading protocol, applied using an easy-to-use knee-loading device (see Appendix), could be developed. This study also uncovers a potential remote stimulatory effect

of mechanical loading, demonstrating that mechanical loads applied at the knee may also strengthen bone in the spine, helping to prevent compression fractures common in osteoporotic patients.

LIST OF REFERENCES

LIST OF REFERENCES

[1] Luiz Carlos Junqueira and Jose Carneiro. *Basic Histology, Text and Atlas*. McGraw-Hill Companies, 10 edition, 2003.

[2] S. Viguet-Carrin, P. Garnero, and P. D Delmas. The role of collagen in bone strength. *Osteoporos Int*, 17(3):319–36, 2006.

[3] T. Bou-Akl, R. Banglmaier, R. Miller, and P Vandevord. Effect of crosslinking on the mechanical properties of mineralized and non-mineralized collagen fibers. *J Biomed Mater Res A*, Jan 28 2013.

[4] R. A. Bank, S. P. Robins, C. Wijmenga, L. J. Breslau-Siderius, A. F. Bardoel, H. A. van der Sluijs, H. E. Pruijs, and J. M TeKoppele. Defective collagen crosslinking in bone, but not in ligament or cartilage, in bruck syndrome: indications for a bone-specific telopeptide lysyl hydroxylase on chromosome 17. *Proc Natl Acad Sci U S A*, 96(3):1054–8, 1999.

[5] M. Saito and K Marumo. Collagen cross-links as a determinant of bone quality: a possible explanation for bone fragility in aging, osteoporosis, and diabetes mellitus. *Osteoporos Int*, 21(2):195–214, 2010.

[6] J. Klein-Nulend and L.F Bonewald. The osteocyte. In J.P. Bilezikian, editor, *Principles of Bone Biology*, volume 1, chapter 8, pages 153–174. Elsevier, London, 2008.

[7] E.F. Morgan and M.L Bouxsein. Biomechanics of bone and age-related fractures. In J.P. Bilezikian, editor, *Principles of Bone Biology*, volume 1, chapter 2, pages 29–52. Elsevier, London, 2008.

[8] L. A. Armas and R. R Recker. Pathophysiology of osteoporosis: new mechanistic insights. *Endocrinol Metab Clin North Am*, 41(3):475–86, 2012.

[9] V. Krishnan, H.U. Bryant, and O.A Macdougald. Regulation of bone mass by wnt signaling. *J Clin Invest*, 116(5):1202–9, 2006.

[10] S. Judex, J. Rubin, and C. T Rubin. Mechanisms of exercise effects on bone quantity and quality. In J.P. Bilezikian, editor, *Principles of Bone Biology*, volume 2, chapter 85, pages 1819–1840. Elsevier, London, 2008.

[11] A. Morrison, T. Fan, S. S. Sen, and L Weisenfluh. Epidemiology of falls and osteoporotic fractures: a systematic review. *Clinicoecon Outcomes Res*, 5:9–18, 2013.

[12] J. L. Old and M Calvert. Vertebral compression fractures in the elderly. *Am Fam Physician*, 69(1):111–6, 2004.

[13] L. A. Nasto, A. Fusco, D. Colangelo, M. Mormando, G. Di Giacomo, B. Rossi, L. De Marinis, C. A. Logroscino, and E. Pola. Clinical predictors of vertebral osteoporotic fractures in post-menopausal women: a cross-sectional analysis. *Eur Rev Med Pharmacol Sci*, 16(9):1227–34, 2012.

[14] M. N. Weitzmann and R Pacifici. Estrogen deficiency and bone loss: an inflammatory tale. *J Clin Invest*, 116(5):1186–94, 2006.

[15] R. Y. Lau and X Guo. A review on current osteoporosis research: with special focus on disuse bone loss. *J Osteoporos*, 2011:293808, 2011.

[16] S. D. Jiang, L. Y. Dai, and L. S Jiang. Osteoporosis after spinal cord injury. *Osteoporos Int*, 17(2):180–92, 2006.

[17] J. Rittweger, H. M. Frost, H. Schiessl, H. Ohshima, B. Alkner, P. Tesch, and D Felsenberg. Muscle atrophy and bone loss after 90 days' bed rest and the effects of flywheel resistive exercise and pamidronate: results from the ltbr study. *Bone*, 36(6):1019–29, 2005.

[18] B. J. Kiratli, A. E. Smith, T. Nauenberg, C. F. Kallfelz, and I Perkash. Bone mineral and geometric changes through the femur with immobilization due to spinal cord injury. *J Rehabil Res Dev*, 37(2):225–33, 2000.

[19] E. Ozcivici, Y. K. Luu, C. T. Rubin, and S Judex. Low-level vibrations retain bone marrow's osteogenic potential and augment recovery of trabecular bone during reambulation. *PLoS One*, 5(6):e11178, 2010.

[20] J. M. Wallace, B. Erickson, C. M. Les, B. G. Orr, and M. M Banaszak Holl. Distribution of type i collagen morphologies in bone: relation to estrogen depletion. *Bone*, 46(5):1349–54, 2010.

[21] M. J Silva. Biomechanics of osteoporotic fractures. *Injury*, 38 Suppl 3:S69–76, 2007.

[22] T. Shibata, A. Shira-Ishi, T. Sato, T. Masaki, A. Masuda, A. Hishiya, N. Ishikura, S. Higashi, Y. Uchida, M. O. Saito, M. Ito, E. Ogata, K. Watanabe, and K Ikeda. Vitamin d hormone inhibits osteoclastogenesis in vivo by decreasing the pool of osteoclast precursors in bone marrow. *J Bone Miner Res*, 17(4):622–9, 2002.

[23] A. Cranney, T. Horsley, S. O'Donnell, H. Weiler, L. Puil, D. Ooi, S. Atkinson, L. Ward, D. Moher, D. Hanley, M. Fang, F. Yazdi, C. Garritty, M. Sampson, N. Barrowman, A. Tsertsvadze, and V Mamaladze. Effectiveness and safety of vitamin d in relation to bone health. *Evid Rep Technol Assess (Full Rep)*, (158):1–235, 2007.

[24] H. A. Bischoff-Ferrari, W. C. Willett, E. J. Orav, P. Lips, P. J. Meunier, R. A. Lyons, L. Flicker, J. Wark, R. D. Jackson, J. A. Cauley, H. E. Meyer, M. Pfeifer, K. M. Sanders, H. B. Stahelin, R. Theiler, and B Dawson-Hughes. A pooled analysis of vitamin d dose requirements for fracture prevention. *N Engl J Med*, 367(1):40–9, 2012.

[25] G Jones. Vitamin d and analogues. In J.P. Bilezikian, editor, *Principles of Bone Biology*, volume 2, chapter 83, pages 1777–1800. Elsevier, London, 2008.

[26] V. A. Moyer. Vitamin d and calcium supplementation to prevent fractures in adults: U.s. preventive services task force recommendation statement. *Ann Intern Med*, Feb 26 2013.

[27] M. J. Bolland, A. Avenell, J. A. Baron, A. Grey, G. S. MacLennan, G. D. Gamble, and I. R Reid. Effect of calcium supplements on risk of myocardial infarction and cardiovascular events: meta-analysis. *BMJ*, 341:c3691, 2010.

[28] I. R. Reid and M. J Bolland. Calcium supplements: bad for the heart? *Heart*, 98(12):895–6, 2012.

[29] S. R. Cummings, J. San Martin, M. R. McClung, E. S. Siris, R. Eastell, I. R. Reid, P. Delmas, H. B. Zoog, M. Austin, A. Wang, S. Kutilek, S. Adami, J. Zanchetta, C. Libanati, S. Siddhanti, and C Christiansen. Denosumab for prevention of fractures in postmenopausal women with osteoporosis. *N Engl J Med*, 361(8):756–65, 2009.

[30] S. Rozenberg, J. Vandromme, and C Antoine. Postmenopausal hormone therapy: risks and benefits. *Nat Rev Endocrinol*, Feb 19 2013.

[31] I Persson. Cancer risk in women receiving estrogen-progestin replacement therapy. *Maturitas*, 23 Suppl:S37–45, 1996.

[32] L. Mosekilde, P. Vestergaard, and L Rejnmark. The pathogenesis, treatment and prevention of osteoporosis in men. *Drugs*, 73(1):15–29, 2013.

[33] J. M. Alexander, I. Bab, S. Fish, R. Muller, T. Uchiyama, G. Gronowicz, M. Nahounou, Q. Zhao, D. W. White, M. Chorev, D. Gazit, and M Rosenblatt. Human parathyroid hormone 1-34 reverses bone loss in ovariectomized mice. *J Bone Miner Res*, 16(9):1665–73, 2001.

[34] J. J. Body, P. Bergmann, S. Boonen, J. P. Devogelaer, E. Gielen, S. Goemaere, J. M. Kaufman, S. Rozenberg, and J. Y Reginster. Extraskeletal benefits and risks of calcium, vitamin d and anti-osteoporosis medications. *Osteoporos Int*, 23 Suppl 1:S1–23, 2012.

[35] H Hagino. Eldecalcitol : newly developed active vitamin d3 analog for the treatment of osteoporosis. *Expert Opin Pharmacother*, 14(6):817–25, 2013.

[36] T. Matsumoto and I Endo. Eldecalcitol for the treatment of osteoporosis. *Drugs Today (Barc)*, 48(3), 2012.

[37] A.J. Roelofs, F.H. Ebetino, A.A. Reszka, G.G. Russell, and M.J Rogers. Biphosphonates: Mechanisms of action. In J.P. Bilezikian, editor, *Principles of Bone Biology*, volume 2, chapter 81, pages 1737–1768. Elsevier, London, 2008.

[38] M. T. Drake, B. L. Clarke, and S Khosla. Bisphosphonates: mechanism of action and role in clinical practice. *Mayo Clin Proc*, 83(9), 2008.

[39] Z Janovska. Bisphosphonate-related osteonecrosis of the jaws. a severe side effect of bisphosphonate therapy. *Acta Medica (Hradec Kralove)*, 55(3):111–5, 2012.

[40] S. O'Donnell, A. Cranney, G. A. Wells, J. D. Adachi, and J. Y. Reginster. Strontium ranelate for preventing and treating postmenopausal osteoporosis. *Cochrane Database Syst Rev*, (4):CD005326, 2006.

[41] P. Bergmann, J. J. Body, S. Boonen, Y. Boutsen, J. P. Devogelaer, S. Goemaere, J. Kaufman, J. Y. Reginster, and S Rozenberg. Loading and skeletal development and maintenance. *J Osteoporos*, 2011:786752, 2010.

[42] S. J Warden. Breaking the rules for bone adaptation to mechanical loading. *J Appl Physiol*, 100(5):1441–2, 2006.

[43] A. Wysocki, M. Butler, T. Shamliyan, and R. L Kane. Whole-body vibration therapy for osteoporosis: state of the science. *Ann Intern Med*, 155(10):680–6, W206–13, 2011.

[44] P. Zhang, M. Su, Y. Liu, A. Hsu, and H Yokota. Knee loading dynamically alters intramedullary pressure in mouse femora. *Bone*, 40(2):538–43, 2007.

[45] P. Zhang, M. Su, S. M. Tanaka, and H Yokota. Knee loading stimulates cortical bone formation in murine femurs. *BMC Musculoskelet Disord*, 7:73, 2006.

[46] S. Weinbaum, S.C. Cowin, and Y Zeng. A model for the excitation of osteocytes by mechanical loading-induced bone fluid shear stresses. *J Biomech*, 27(3):339–60, 1994.

[47] D.P. Nicolella, D.E. Moravits, A.M. Gale, L.F. Bonewald, and J Lankford. Osteocyte lacunae tissue strain in cortical bone. *J Biomech*, 39(3):1735–43, 2006.

[48] L.F Bonewald. Mechanosensation and transduction in osteocytes. *Bonekey Osteovision*, 3(10):7–15, 2006.

[49] N. Stolzenberg, D. L. Belavy, G. Beller, G. Armbrecht, J. Semler, and D Felsenberg. Bone strength and density via pqct in post-menopausal osteopenic women after 9 months resistive exercise with whole body vibration or proprioceptive exercise. *J Musculoskelet Neuronal Interact*, 13(1), 2013.

[50] A. M. Weatherholt, R. K. Fuchs, and S. J Warden. Cortical and trabecular bone adaptation to incremental load magnitudes using the mouse tibial axial compression loading model. *Bone*, 52(1):372–9, 2013.

[51] R. L. De Souza, M. Matsuura, F. Eckstein, S. C. Rawlinson, L. E. Lanyon, and A. A Pitsillides. Non-invasive axial loading of mouse tibiae increases cortical bone formation and modifies trabecular organization: a new model to study cortical and cancellous compartments in a single loaded element. *Bone*, 37(6):810–8, 2005.

[52] P. Zhang and H Yokota. Knee loading stimulates healing of mouse bone wounds in a femur neck. *Bone*, 49(4):867–72, 2011.

[53] S. W. Donahue, C. R. Jacobs, and H. J Donahue. Flow-induced calcium oscillations in rat osteoblasts are age, loading frequency, and shear stress dependent. *Am J Physiol Cell Physiol*, 281(5):C1635–41, 2001.

[54] Y. F. Hsieh and C. H Turner. Effects of loading frequency on mechanically induced bone formation. *J Bone Miner Res*, 16(5):918–24, 2001.

[55] P. Zhang, S. M. Tanaka, Q. Sun, C. H. Turner, and H Yokota. Frequency-dependent enhancement of bone formation in murine tibiae and femora with knee loading. *J Bone Miner Metab*, 25(6):383–91, 2007.

[56] Y. Kameo, T. Adachi, and M Hojo. Effects of loading frequency on the functional adaptation of trabeculae predicted by bone remodeling simulation. *J Mech Behav Biomed Mater*, 4(6):900–8, 2011.

[57] S. M. Tanaka, I. M. Alam, and C. H Turner. Stochastic resonance in osteogenic response to mechanical loading. *FASEB J*, 17(2):313–4, 2003.

[58] S. J. Warden and C. H Turner. Mechanotransduction in the cortical bone is most efficient at loading frequencies of 5-10 hz. *Bone*, 34(2):261–70, 2004.

[59] Y. X. Qin and H Lam. Intramedullary pressure and matrix strain induced by oscillatory skeletal muscle stimulation and its potential in adaptation. *J Biomech*, 42(2):140–5, 2009.

[60] M. P. Akhter, G. K. Alvarez, D. M. Cullen, and R. R Recker. Disuse-related decline in trabecular bone structure. *Biomech Model Mechanobiol*, 10(3):423–9, 2011.

[61] H Sievanen. Immobilization and bone structure in humans. *Arch Biochem Biophys*, 503(1):146–52, 2010.

[62] H. Yokota and S. M Tanaka. Osteogenic potentials with joint-loading modality. *J Bone Miner Metab*, 23(4):302–8, 2005.

[63] M. Inada, C. Matsumoto, and C Miyaura. [animal models for bone and joint disease. ovariectomized and orchidectomized animals]. *Clin Calcium*, 21(2):164–70, 2011.

[64] I. Orlic, F. Borovecki, P. Simic, and S Vukicevic. Gene expression profiling in bone tissue of osteoporotic mice. *Arh Hig Rada Toksikol*, 58(1):3–11, 2007.

[65] J. O. Strom, A. Theodorsson, E. Ingberg, I. M. Isaksson, and E Theodorsson. Ovariectomy and 17beta-estradiol replacement in rats and mice: a visual demonstration. *J Vis Exp*, (64):e4013, 2012.

[66] J. McMillan, R. C. Kinney, D. M. Ranly, S. Fatehi-Sedeh, Z. Schwartz, and B. D Boyan. Osteoinductivity of demineralized bone matrix in immunocompromised mice and rats is decreased by ovariectomy and restored by estrogen replacement. *Bone*, 40(1):111–21, 2007.

[67] L. Zhao, J. W. Shim, T. R. Dodge, A. G. Robling, and H Yokota. Inactivation of lrp5 in osteocytes reduces young's modulus and responsiveness to the mechanical loading. *Bone*, 54(1):35–43, 2013.

[68] A. Eddleston, M. Marenzana, A. R. Moore, P. Stephens, M. Muzylak, D. Marshall, and M. K Robinson. A short treatment with an antibody to sclerostin can inhibit bone loss in an ongoing model of colitis. *J Bone Miner Res*, 24(10):1662–71, 2009.

[69] S. M. Tanaka, H. B. Sun, and H Yokota. Bone formation induced by a novel form of mechanical loading on joint tissue. *Biol Sci Space*, 18(2):41–4, 2004.

[70] J. I. Aguirre, L. I. Plotkin, S. A. Stewart, R. S. Weinstein, A. M. Parfitt, S. C. Manolagas, and T Bellido. Osteocyte apoptosis is induced by weightlessness in mice and precedes osteoclast recruitment and bone loss. *J Bone Miner Res*, 21(4):605–15, 2006.

[71] F. Sugiyama, J. Wu, M. Fujioka, J. Ezaki, K. Takeda, C. Miyaura, T. Ishida, K. Yamada, and Y Ishimi. Soybean isoflavones preserve bone mass in hindlimb-unloaded mice. *J Bone Miner Metab*, 24(6):439–46, 2006.

[72] J. Yamashita, X. Li, B. R. Furman, H. R. Rawls, X. Wang, and C. M Agrawal. Collagen and bone viscoelasticity: a dynamic mechanical analysis. *J Biomed Mater Res*, 63(1):31–6, 2002.

[73] A. Tsuchikane, Y. Nakatsuchi, and A Nomura. The influence of joints and soft tissue on the natural frequency of the human tibia using the impulse response method. *Proc Inst Mech Eng H*, 209(3):149–55, 1995.

[74] N. L. Chattah, A. Sharir, S. Weiner, and R Shahar. Determining the elastic modulus of mouse cortical bone using electronic speckle pattern interferometry (espi) and micro computed tomography: a new approach for characterizing small-bone material properties. *Bone*, 45(1):84–90, 2009.

[75] L. X. Guo, M. Zhang, Y. M. Zhang, and E. C Teo. Vibration modes of injured spine at resonant frequencies under vertical vibration. *Spine (Phila Pa 1976)*, 34(19):E682–8, 2009.

[76] W. R. Taylor, E. Roland, H. Ploeg, D. Hertig, R. Klabunde, M. D. Warner, M. C. Hobatho, L. Rakotomanana, and S. E Clift. Determination of orthotropic bone elastic constants using fea and modal analysis. *J Biomech*, 35(6):767–73, 2002.

[77] T. K. Hight, R. L. Piziali, and D. A Nagel. Natural frequency analysis of a human tibia. *J Biomech*, 13(2), 1980.

[78] F. Linde, I. Hvid, and B Pongsoipetch. Energy absorptive properties of human trabecular bone specimens during axial compression. *J Orthop Res*, 7(3):432–9, 1989.

[79] J. Yamashita, B. R. Furman, H. R. Rawls, X. Wang, and C. M Agrawal. The use of dynamic mechanical analysis to assess the viscoelastic properties of human cortical bone. *J Biomed Mater Res*, 58(1):47–53, 2001.

[80] M. D. Martinez, G. J. Schmid, J. A. McKenzie, D. M. Ornitz, and M. J Silva. Healing of non-displaced fractures produced by fatigue loading of the mouse ulna. *Bone*, 46(6):1604–12, 2010.

[81] A. G. Robling, P. J. Niziolek, L. A. Baldridge, K. W. Condon, M. R. Allen, I. Alam, S. M. Mantila, J. Gluhak-Heinrich, T. M. Bellido, S. E. Harris, and C. H Turner. Mechanical stimulation of bone in vivo reduces osteocyte expression of sost/sclerostin. *J Biol Chem*, 283(9):5866–75, 2008.

[82] S. J. Warden, A. G. Robling, M. S. Sanders, M. M. Bliziotes, and C. H Turner. Inhibition of the serotonin (5-hydroxytryptamine) transporter reduces bone accrual during growth. *Endocrinology*, 146(2):685–93, 2005.

[83] A. M. Parfitt, M. K. Drezner, F. H. Glorieux, J. A. Kanis, H. Malluche, P. J. Meunier, S. M. Ott, and R. R Recker. Bone histomorphometry: standardization of nomenclature, symbols, and units. report of the asbmr histomorphometry nomenclature committee. *J Bone Miner Res*, 2(6):595–610, 1987.

[84] A. P. Fortis, V. Kostopoulos, E. Panagiotopoulos, S. Tsantzalis, and A Kokkinos. Viscoelastic properties of cartilage-subchondral bone complex in osteoarthritis. *J Med Eng Technol*, 28(5):223–6, 2004.

[85] R Lakes. *Viscoelastic Solids*. CRC Press, Boca Raton, FL, 1999.

[86] T. D Weaver. The shape of the neandertal femur is primarily the consequence of a hyperpolar body form. *Proc Natl Acad Sci U S A*, 100(12):6926–9, 2003.

[87] A. A Biewener. Musculoskeletal design in relation to body size. *J Biomech*, 24 Suppl 1:19–29, 1991.

[88] J. E. Bertram and A. A Biewener. Bone curvature: sacrificing strength for load predictability? *J Theor Biol*, 131(1):75–92, 1988.

[89] R. P. Main, M. E. Lynch, and M. C van der Meulen. In vivo tibial stiffness is maintained by whole bone morphology and cross-sectional geometry in growing female mice. *J Biomech*, 43(14):2689–94, 2010.

[90] R. Y. Kwon, D. R. Meays, A. S. Meilan, J. Jones, R. Miramontes, N. Kardos, J. C. Yeh, and J. A Frangos. Skeletal adaptation to intramedullary pressure-induced interstitial fluid flow is enhanced in mice subjected to targeted osteocyte ablation. *PLoS One*, 7(3):e33336, 2012.

[91] H. Lam, P. Brink, and Y. X Qin. Skeletal nutrient vascular adaptation induced by external oscillatory intramedullary fluid pressure intervention. *J Orthop Surg Res*, 5:18, 2010.

[92] S. J. Sample, M. Behan, L. Smith, W. E. Oldenhoff, M. D. Markel, V. L. Kalscheur, Z. Hao, V. Miletic, and P Muir. Functional adaptation to loading of a single bone is neuronally regulated and involves multiple bones. *J Bone Miner Res*, 23(9):1372–81, 2008.

[93] T. Dodge, M. Wanis, R. Ayoub, L. Zhao, N. B. Watts, A. Bhattacharya, O. Akkus, A. Robling, and H Yokota. Mechanical loading, damping, and load-driven bone formation in mouse tibiae. *Bone*, 51(4):810–8, 2012.

[94] K. J. Kim and I.K Hwang. Prediction of resonance characteristics of the forearm bones using finite element analysis. *J Musculoskelet Res*, 10(4):205–215, 2006.

[95] M. Fondrk, E. Bahniuk, D. T. Davy, and C Michaels. Some viscoplastic characteristics of bovine and human cortical bone. *J Biomech*, 21(8):623–30, 1988.

[96] V. David, A. Martin, M. H. Lafage-Proust, L. Malaval, S. Peyroche, D. B. Jones, L. Vico, and A Guignandon. Mechanical loading down-regulates peroxisome proliferator-activated receptor gamma in bone marrow stromal cells and favors osteoblastogenesis at the expense of adipogenesis. *Endocrinology*, 148(5):2553–62, 2007.

[97] Y.H. Kim, C.H. Byun, and T.Y Oh. Effect of osteoporosis on natural frequencies in mouse femur: Vibration test and micro-ct based finite element analysis. *Key Eng Mater*, 326-328:851–854, 2006.

[98] M. C. Hobatho, R. Darmana, P. Pastor, J. J. Barrau, S. Laroze, and J. P Morucci. Development of a three-dimensional finite element model of a human tibia using experimental modal analysis. *J Biomech*, 24(6):371–83, 1991.

[99] Q. Wan, S. J. Kim, H. Yokota, and S Na. Differential activation and inhibition of rhoa by fluid flow induced shear stress in chondrocytes. *Cell Biol Int*, Feb 13 2013.

[100] M. D. Schofer, J. E. Block, J. Aigner, and A Schmelz. Improved healing response in delayed unions of the tibia with low-intensity pulsed ultrasound: results of a randomized sham-controlled trial. *BMC Musculoskelet Disord*, 11:229, 2010.

APPENDIX

APPENDIX: HUMAN-SCALE KNEE LOADING DEVICE

As demonstrated in this thesis, lateral loading of the knee joint has shown positive results in animal studies in increasing bone density and mechanical properties in nearby bones, such as the femur and tibia, in addition to more remote locations, such as the spine. The ultimate goal of this research is to lead the development of a treatment modality that can be used safely and effectively in osteoporotic patients, reducing the harmful side effects observed in some current treatments.

Development of a human-scale knee loading device is the first step in making the jump from animal studies to clinical trials. In an effort to increase patient compliance, a human-scale knee loading device should be portable, so that it may be used outside of a hospital setting, and easy to use by patients of all sizes and backgrounds. Several devices have been produced as bone stimulating devices for restorative purposes. These devices primarily use vibration to accomplish bone cell stimulation [49, 100]. However, to my knowledge, no human-scale knee loading device has been developed for use in clinical trials.

To accomplish knee loading at a human scale and meet the design constrictions, a device was constructed. This effort was a team collaboration involving faculty and students from multiple departments, and my primary responsibilities involved material selection, device optimization, and validation. The device is powered by a moving magnet voice coil motor that can provide linear movement with a force range of 0 N to 10 N at a frequency range of 1 to 20 Hz (Non-Comm Moving Magnet Actuator, H2W Technologies, Inc., Santa Clarita, CA). Structural components are composed of aluminum, and the drivetrain linkage is structural steel. The loading pads and

outside case are made from high-density polyethylene. All materials were chosen to provide the best balance of low weight and suitable strength for the application. The voice coil actuator is driven by a microcontroller with an amplifier circuit powered by a 5 V power supply. The microcontroller allowed programming of the control panel push buttons, which allow the selection of a loading force, frequency, and treatment time.

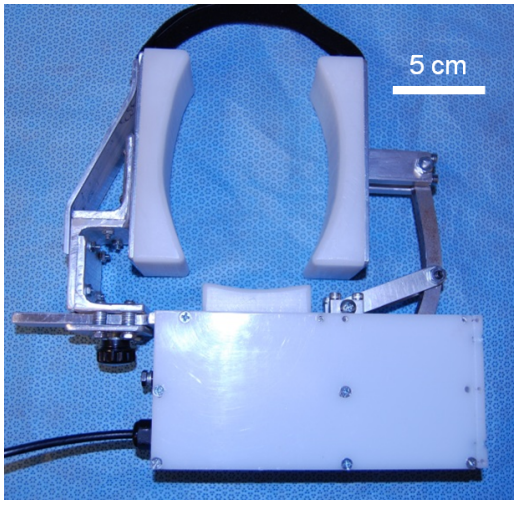

(a) Human-scale knee loading device prototype.

(b) Microcontroller control panel with push buttons and status screen.

While the device is relatively maneuverable, it still relies on plug-in power and may be too heavy for some patients to effectively use. Therefore, in the future, advanced

models of this prototype may implement battery power, and eliminate the need for a separate control panel. In addition, a smaller motor may become available in the future, reducing weight and increasing effectiveness.

In this thesis, the analysis of the properties of bone under dynamic loading conditions demonstrated a relationship between the locations of observed bone formation and the resonant characteristics of the bone structure. Loading at a resonant frequency may increase the effects of localized bending moments within the bone, maximizing bone formation in specific areas. In the future, studies linking this phenomenon and trials from a human-scale knee loading device may lead to the ability to develop a patient-specific loading regimen based on non-invasive imaging and *in-silico* analysis.